

Stable Multivariate Functional Time Series Prediction for Major Geomagnetic Indices

Yian Yu¹, Shasha Zou², Tuija Pulkkinen², and Yang Chen^{*1}

¹Department of Statistics, University of Michigan, Ann Arbor, MI, USA

²Department of Climate and Space Sciences and Engineering, University of Michigan, Ann Arbor, MI, USA

June 15, 2026

Abstract

High-resolution scientific data, such as geomagnetic index streams, often exhibit complex temporal dependencies that can be modeled through functional data analysis. Conventional functional time series (FTS) methods typically partition continuous processes into non-overlapping segments, which artificially fragments temporal continuity and can limit estimation efficiency and stability. This is particularly evident in geomagnetic time series prediction due to their noisy, sudden, large-scale changes. This study presents a robust multivariate FTS forecasting framework for multi-dimensional time series with inter-series correlations and the existence of exogenous predictors. We introduce an overlapping rolling-window scheme that preserves temporal coherence and mitigates boundary information loss, thereby enriching the effective sample size for a more efficient and stable estimation. We integrate functional principal component analysis for dimension reduction with a vector autoregressive model with exogenous inputs to capture latent dynamics across correlated series. We also construct computationally efficient conformal prediction intervals for uncertainty quantification. The framework is motivated by and applied to the simultaneous forecasting of five critical geomagnetic indices, Kp, Dst, SYM-H, SME, SMR, using solar wind parameters as predictors. Empirical results show that this approach outperforms state-of-the-art machine learning baselines, extends forecast horizons to 6–24 hours, and provides calibrated uncertainty bounds.

Keywords: Overlapping rolling-window; Conformal prediction; Geomagnetic indices forecasting

*Corresponding author: ychenang@umich.edu

1 Introduction

Advances in sensor technology and automated data acquisition have facilitated the collection of high-resolution observations in many scientific domains. The field of space weather forecasting has witnessed a strong boom of physics-informed data-driven approaches over the past two decades due to the availability of large volumes of streaming satellite data collected at high spatial and temporal resolutions (Camporeale 2019, Chen et al. 2024). With constant observations of solar activity and near-Earth magnetosphere, ionosphere, and thermosphere conditions, scientists are faced with a gigantic volume of data that can potentially improve forecasting accuracy, lead time, and reliability for many different space weather events. Among them, geomagnetic activity (created by solar and solar wind variations, such as solar storm) is monitored through multiple indices that summarize different aspects of the coupled magnetosphere-ionosphere system and are recorded continuously over time, which are closely associated with risks to power grids, satellite navigation and communication system, and satellites electronics (Sokolova et al. 2021, Xue et al. 2024). Together with near-Earth solar-wind measurements, these observations form a collection of strongly dependent and heterogeneous time series with distinct temporal resolutions, dynamic ranges, and storm-time variability, as illustrated in Figure 1. The figure shows strong temporal dependence within individual series, including persistence, abrupt storm-time transitions, extended recovery behavior, and cross-variable co-variation during active intervals. It also illustrates substantial heterogeneity across variables in scale, smoothness, intermittency, and dynamic range: some series evolve gradually, whereas others are characterized by sharp bursts or highly irregular fluctuations.

Although several variables exhibit similar patterns during periods of disturbance, forecasting remains difficult because only information available up to the forecast time can be used. The model must therefore learn lagged and evolving dependencies rather than rely on contemporaneous alignment, which is visible only in retrospect. Existing data-driven studies on geomagnetic index forecasting frame the time series prediction problem as a classical machine learning task and are largely designed for individual index prediction, with forecasting skill often limited to short lead times of roughly 1–3 hours (Chandorkar et al. 2017, Laperre et al. 2020, Park et al. 2021, Iong et al. 2022, Hu et al. 2023, Iong et al. 2024, Chen et al. 2025). Despite promising root mean square error (RMSE) results, such works

either fail to capture longer-range temporal dependency or are computationally expensive given the temporal dependencies; thus, this inaccurate characterization of the data results in less reliable out-of-sample forecasts. These limitations motivate a functional perspective, in which short temporal segments are treated as curves, and their sequential evolution is modeled over time.

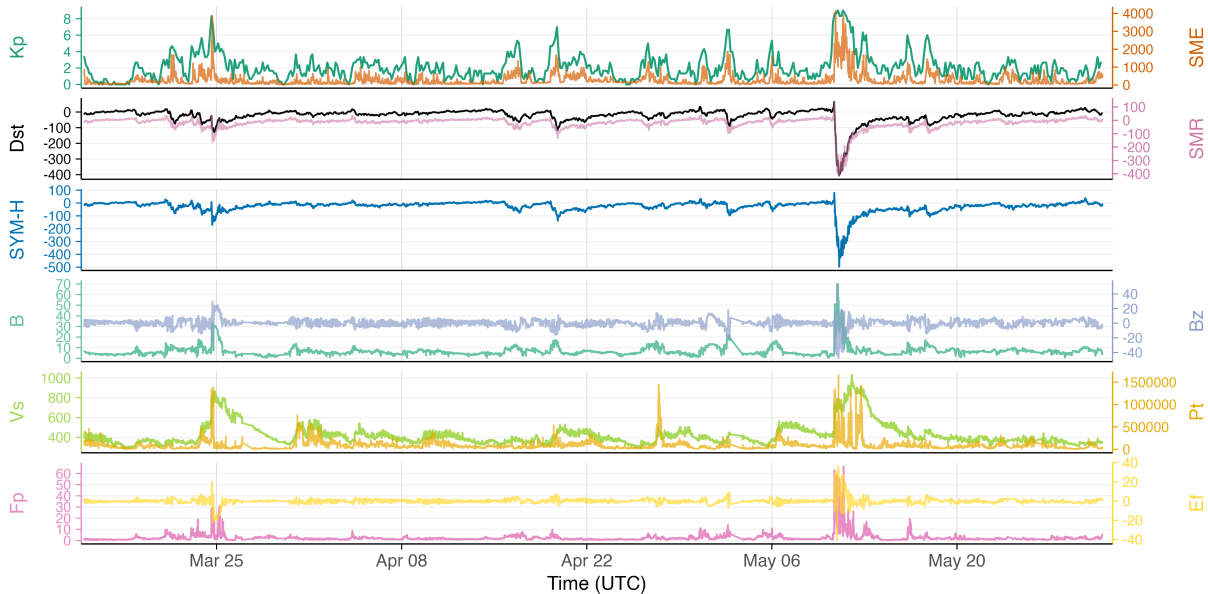


Figure 1: Representative time series of the geomagnetic indices Kp, Dst, SYM-H, SME, and SMR together with the near-Earth solar-wind and interplanetary magnetic field (IMF) variables B, Bz, Vs, Pt, Fp, and Ef over a selected interval in 2024.

1.1 Functional Time Series: Brief Literature

Functional data analysis (FDA) treats individual observations as realizations of smooth functions, such as curves, images, or surfaces, rather than finite-dimensional vectors (Ramsay & Silverman 2005). Typical examples include growth curves (Erbas et al. 2007), environment pollution concentration (Aue et al. 2015), electricity consumption (Antoniadis et al. 2006a, Shang 2013), and movement trajectories (Yu et al. 2024, Gertheiss et al. 2024). Functional time series (FTS) arise when such functional observations are collected sequentially over time and are modeled as a stochastic process.

Hyndman & Ullah (2007) introduced a foundational FTS forecasting framework via functional principal component analysis (FPCA), where principal component (PC) scores are

extracted from curves, forecasted in a lower-dimensional space, and then used to reconstruct future trajectories. This framework has motivated extensions such as robust variants for handling outliers (Shang 2019) and functional ARMAX models that incorporate moving-average terms (González et al. 2017). Other decomposition-based methodologies include singular spectrum analysis (SSA), adapted to functional (Hagbin et al. 2021, Trinka et al. 2023) and multivariate FTS contexts (Trinka et al. 2022), alongside similarity-based methods employing k -nearest neighbors (Antoniadis et al. 2006b) or pattern sequence matching (Bokde et al. 2017). Nonetheless, scalable multivariate FTS with exogenous functional covariates remains challenging, especially when the observed series are noisy, heterogeneous, and strongly dependent.

1.2 Our Contribution: OLFTSA

We propose a new multivariate FTS forecasting framework with exogenous regressors for high-resolution, heterogeneous, and strongly dependent geomagnetic index data observed together with solar-wind drivers. Our approach extends Hyndman & Ullah (2007) by applying FPCA separately to each smoothed functional variable, rotating the stacked score matrix via orthogonal varimax for interpretability and parsimony Kaiser (1958), and model the resulting scores jointly through a vector autoregressive framework with exogenous inputs. This yields an estimation and forecasting procedure that is robust to heterogeneous resolutions, varied noise levels, and inconsistent fluctuation magnitudes across series. We refer to the proposed method as **Overlapping Functional Time Series Analysis** with conformal prediction, denoted as **OLFTSA**, throughout the rest of the paper.

Another distinctive feature of OLFTSA is the use of overlapping rolling windows to construct functional segments from the original time series; see Figure 2. In contrast to conventional FTS approaches that partition continuous-time data into non-overlapping segments (e.g., by day, week, or year), this design preserves temporal continuity across adjacent segments, avoid losing transitional behavior at window boundaries, and enriches the effective sample size. Simulation studies in Section 3.4 show improved forecasting performance relative to non-overlapping constructions. This overlapping structure also facilitates the uncertainty quantification procedure developed in Section 3.3, providing distribution-free validity under modest exchangeability conditions with tractable computation. We apply

OLFTSA to the joint forecasting of multiple geomagnetic indices using solar-wind drivers and show that it delivers competitive 6–24 hour forecasts in real-data experiments, extending beyond the roughly 3-hour horizons typical of most existing single-index models constrained by the decay and complexity of solar wind forcing (Khabarova & Price 2024).

The rest of the manuscript is organized as follows. Section 2 gives the construction of functional data with geomagnetic indices as responses and solar-wind parameters as predictors. Section 3 presents the proposed model. Section 3.1 outlines the FTS methodological foundations. Section 3.4 and Section 4 present simulations studies and real-data applications with benchmarks, respectively. Section 5 is the conclusion. Additional tables, figures, and theoretical proofs are provided in the Online Supplementary Materials.

2 Geomagnetic Index Prediction Data

This study considers the joint forecasting of multiple geomagnetic indices using near-Earth solar wind and interplanetary magnetic field (IMF) measurements as predictors. The target indices, Kp, Dst, SYM-H, SME, and SMR, are crucial to space weather operations, serving as proxies for distinct magnetospheric current systems across varying temporal scales. Despite sharing a common primary driver in solar wind-magnetosphere interaction (Newell et al. 2007), these indices exhibit substantial heterogeneity in both sampling cadence and dynamic range. Consequently, studies in literature typically treat them as separate tasks (Camporeale 2019). These indices exhibit non-negligible within-index and cross-index correlations, as shown in Figure B.1 in the Online Supplementary Materials, which motivates a joint model.

The target variables are five widely used geomagnetic indices: Kp from GFZ Potsdam (<https://kp.gfz.de/>), Dst and SYM-H from WDC Kyoto (<https://wdc.kugi.kyoto-u.ac.jp/>), and SME and SMR from SuperMAG (<https://supermag.jhuapl.edu/>). Together, these indices characterize complementary aspects of geomagnetic activity across different temporal scales and current systems. Specifically, Kp is a planetary index of global geomagnetic activity derived from mid-latitude ground magnetometers and reported every 3 hours. Dst is the disturbance storm-time index, which measures the intensity of the ring current using low-latitude magnetic observations at hourly cadence. SYM-H is a 1-minute high-temporal-

resolution analogue of Dst, allowing finer characterization of rapid storm-time variations. SME is a high-latitude auroral electrojet index that quantifies auroral-zone horizontal ionospheric current activity and is particularly informative for substorm dynamics. SMR is a SuperMAG ring-current index analogous to Dst and SYM-H but constructed from a broader station network, providing improved spatial coverage.

The response set spans 1995–2025 and combines variables observed at heterogeneous cadences, ranging from 3-hourly Kp to hourly Dst and minute-level SYM-H, SME, and SMR. These indices also differ substantially in scale and dynamical behavior; for example, Kp ranges from 0 to 9, whereas SME may exceed 6000 nT during major geomagnetic disturbances. The high-frequency variables also exhibit short-scale variability and occasional redundancy at fine temporal resolution, motivating preprocessing before functional reconstruction. To reduce noise and eliminate near-duplicate adjacent observations at very fine resolution, we computed 5-minute averages for SYM-H, SME, and SMR (Long et al. 2022).

The predictor set comprises six solar wind and IMF variables commonly used in geomagnetic index forecasting. Emphasis is placed on the southward IMF Bz, which governs dayside magnetic reconnection and energy input into the magnetosphere. Additionally, derived quantities such as the plasma flow dynamic pressure and solar wind motional electric field are included to capture known nonlinearities in solar wind magnetosphere coupling. More precisely, the predictor consists of solar wind and IMF parameters from NASA’s OMNIWeb database (<https://omniweb.gsfc.nasa.gov/>), which is widely used in geomagnetic forecasting studies; see, for example, Fung & Shao (2008), Ayala Solares et al. (2016), Wang et al. (2023), Long et al. (2022), Nair et al. (2023), Polozov (2023). In this study, we focus on a subset of predictors selected by examining cross-covariance with the target indices at multiple time lags; see Figure B.2 in the Online Supplementary Materials. The selected variables are total IMF magnitude (B in nT), IMF component in the north-south direction in Geocentric Solar Magnetospheric (GSM) coordinates (Bz in nT; critical for magnetic reconnection), plasma flow speed (Vs in Km/s), proton temperature (Pt in K), flow dynamic pressure (Fp in nPa), and motional electric field (Ef in mV/m).

The OMNI predictors are available over 1995–2025 at high temporal resolution, including 1-minute products, but contain occasional missing values and are not directly aligned with the heterogeneous cadences of the response variables. To standardize the temporal grid

and reduce preprocessing complexity, we linearly interpolated isolated missing values and resampled all OMNI predictors to 1-hour resolution. A summary table of the response and predictor variables is shown in Table B.1 in the Online Supplementary Materials.

3 Model Architecture and Validation

3.1 Functional PCA (FPCA)

We assume that the observations arise from an underlying smooth FTS, $y_d(t_i) = y_d(t_i) + \varepsilon_{d,i}$, for $i = 1, \dots, n$, $d = 1, \dots, D$, where $\{t_i\}_{i=1}^n \subset \mathcal{T}$ are sampling points where the trajectories are measured, and $\varepsilon_{d,i}$ are independent and identically distributed (i.i.d.) measurement errors with mean zero and variance σ_ε^2 . For discretely observed trajectories contaminated by noise, smoothing is typically used to recover the latent functional structure before estimating the mean and covariance functions. For densely observed trajectories, one may presmooth each curve using spline or local kernel methods; for sparse designs, the mean and covariance can be instead estimated by pooling information across subjects (Yao et al. 2005). After smoothing, we still denote the reconstructed trajectories by $\{y_d\}_{d=1}^D$ for notational simplicity. The mean function and covariance kernel are estimated by

$$\hat{\mu}(t) = \frac{1}{D} \sum_{d=1}^D y_d(t), \quad t \in \mathcal{T}, \quad \text{and} \quad \hat{\mathcal{C}}(t, s) = \frac{1}{D} \sum_{d=1}^D (y_d(t) - \hat{\mu}(t))(y_d(s) - \hat{\mu}(s)).$$

Under weak stationarity, the lag-0 autocovariance operator \mathcal{C} associated with $\{y_d, d \in \mathbb{N}\}$ is a nonnegative, self-adjoint Hilbert-Schmidt operator on \mathcal{H} . By Mercer's theorem, it admits the spectral decomposition $\mathcal{C}(\cdot) = \sum_{k=1}^{\infty} \lambda_k \langle \phi_k, \cdot \rangle \phi_k$, where $\{\lambda_k, k \in \mathbb{N}\}$ is a nonincreasing sequence of eigenvalues and $\{\phi_k, k \in \mathbb{N}\}$ are the corresponding orthonormal eigenfunctions satisfying $\mathcal{C}(\phi_k) = \lambda_k \phi_k$ and $\|\phi_k\| = 1$ (Ash & Gardner 1975, Hsing & Eubank 2015). This yields the Karhunen-Lové expansion (Gohberg et al. 2012) $y_d(t) = \mu(t) + \sum_{k=1}^{\infty} \xi_{d,k} \phi_k(t)$, $\xi_{d,k} := \langle y_d - \mu, \phi_k \rangle$, $t \in \mathcal{T}$, where μ is the mean function. Scores $\xi_{d,k}$ are uncorrelated random variables with zero mean and variance λ_k . Truncating the expansion at K terms yields a finite-dimensional approximation in which the leading components often capture most of the variation in the sample paths (Ramsay & Silverman 2005, Horváth & Kokoszka 2012). Unlike spline, Fourier, or wavelet expansions, FPCA uses the eigenfunctions of the covariance operator as a data-adaptive basis, which achieves effective dimension reduction

with relatively few components (Horváth & Kokoszka 2012). The eigenvalues $\{\hat{\lambda}_k\}_{k=1}^K$ and eigenfunctions $\{\hat{\phi}_k\}_{k=1}^K$ are obtained from the spectral decomposition of $\hat{\mathcal{C}}$. Under standard regularity assumptions, they are consistent at rate $D^{-1/2}$ (Bosq 2000). The measurement error variance is estimated by

$$\hat{\sigma}_\varepsilon^2 = \frac{1}{D} \sum_{d=1}^D \frac{1}{n} \sum_{i=1}^n \left[\left(y_d(t_i) - \frac{1}{n} \sum_{i=1}^n y_d(t_i) \right)^2 - \hat{\mathcal{C}}(t_i, t_i) \right].$$

Choosing K remains application dependent. Common approaches include scree plots and the explained cumulative proportion of variance (Jolliffe 2002). Implementations are available in the R packages `fda` and `refund` (Ramsay et al. 2009, Goldsmith et al. 2013).

3.2 OLFTSA Model Description

Building on the functional representation of geomagnetic indices and solar wind drivers, we propose a framework that combines patch-wise functional preprocessing with an overlapping rolling-window scheme, FPCA-based dimension reduction, and multivariate time series forecasting with exogenous inputs to produce multi-step forecasts of future index curves (patches), as summarized in Figure 2. The framework is designed to accommodate heterogeneous sampling cadences and fluctuation magnitudes across variables by operating on smoothed functional patches and forecasting in a low-dimensional score space.

Let $\{y_p(t_i), i \in \mathbb{N}\}$ denote the raw observation stream for variable p , where $p \in \mathcal{P} \cup \mathcal{Q}$, $\mathcal{P} = \{\text{kp, Dst, SYM-H, SME, SMR}\}$ denotes the set of target variables, and $\mathcal{Q} = \{\text{B, Bz, Vs, Pt, Fp, Ef}\}$ is the set of input solar wind plasma features. The observations are reshaped into fixed-duration patches, such as 48- or 72-hour windows, indexed by $d = 1, \dots, D$. Denote the d -th patch for variable p by $y_{p,d}(t_{p,1}), \dots, y_{p,d}(t_{p,n_p})$, where $\{t_{p,i}\}_{i=1}^{n_p} \subset \mathcal{T}$ is the within-patch time grid, which may differ across variables. Empirical autocorrelation decays substantially within about one day across variables, see Figure B.1 in the Online Supplementary Materials, this motivates the use of overlapping rolling windows to preserve short-range dependence across adjacent patches.

Each patch is treated as a discretely observed realization of an underlying smooth function on \mathcal{T} , and smoothing, for example with penalized B-splines, is used to obtain a functional estimate $y_{p,d}(\cdot)$. Applying the FPCA construction in Section 3.1 separately to each variable

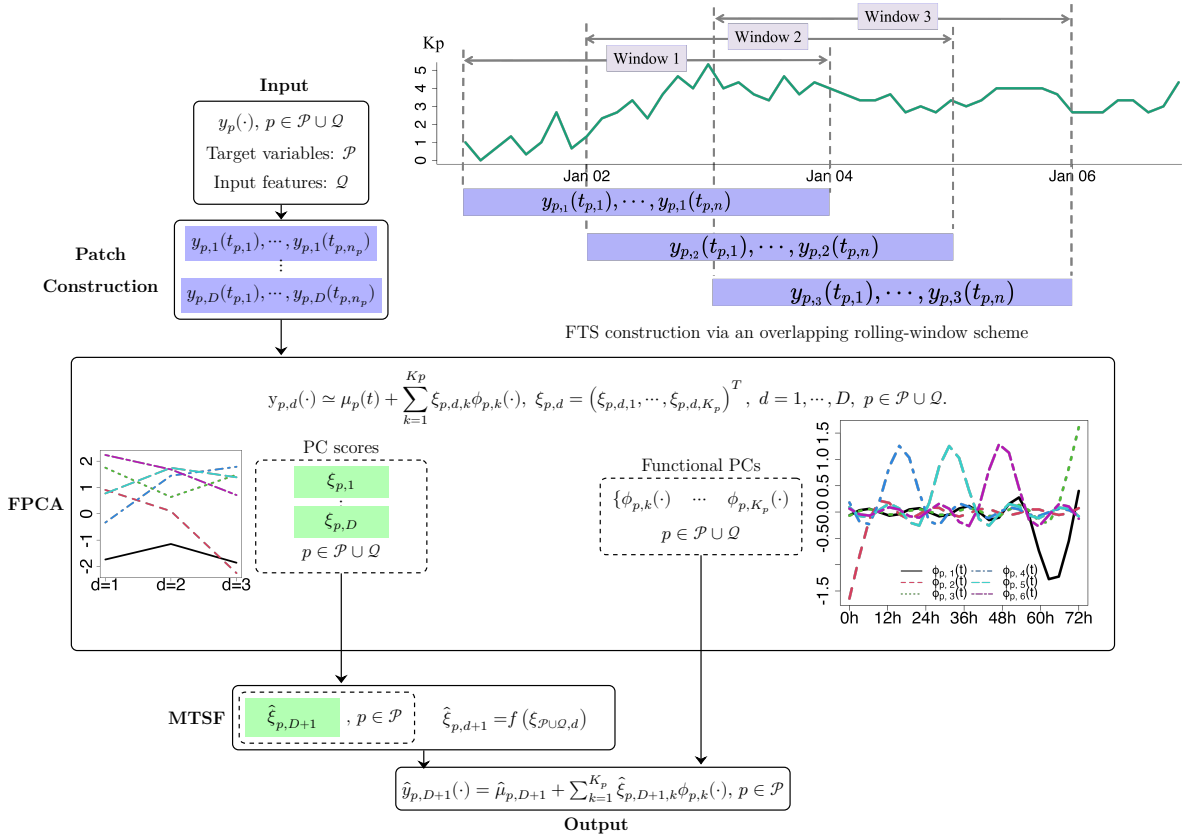


Figure 2: Schematic illustration of the proposed OLFTSA framework. The embedded plots use K_p as an illustrative example to explain the overlapping rolling-window construction and the associated FPCA quantities. \mathcal{P} is the set of target geometric indices and \mathcal{Q} is the set of input solar-wind and IMF features; specifically $\mathcal{P} = \{K_p, \text{Dst}, \text{SYM-H}, \text{SME}, \text{SMR}\}$ and $\mathcal{Q} = \{B, B_z, V_s, P_t, F_p, E_f\}$. FPCA denotes functional principal components analysis, and MTSF denotes multivariate time series forecasting.

p yields eigenfunctions $\{\phi_{p,k}(\cdot)\}_{k \geq 1}$ and scores $\{\xi_{p,d,k}\}_{k \geq 1}$. Truncation to K_p components gives a finite-dimensional representation, where K_p is chosen by a pre-specified proportion of explained variance, for example 0.99, with $K_p \leq n_p$.

Let $\xi_{p,d} = (\xi_{p,d,1}, \dots, \xi_{p,d,K_p})^\top$ denote the functional PC score vector for variable p at patch d , for $d = 1, \dots, D$. Stacking scores across targets \mathcal{P} and predictors \mathcal{Q} yields the multivariate score time series $\{\xi_{\mathcal{P} \cup \mathcal{Q},d}\}_{d=1}^D$. A multivariate time series forecasting model with exogenous inputs is then fitted to capture temporal dependence and cross-variable interactions, and is used to predict the next-patch scores $\hat{\xi}_{p,d+1}$ for $p \in \mathcal{P}$. More generally, we write $\hat{\xi}_{p,d+1} = f(\xi_{\mathcal{P} \cup \mathcal{Q},d}, \dots, \xi_{\mathcal{P} \cup \mathcal{Q},d-h})$, where f is a forecasting map and h is the lag order. In the empirical analysis, lagged correlation decays rapidly, so we use only the most recent patch, $\hat{\xi}_{p,d+1} = f(\xi_{\mathcal{P} \cup \mathcal{Q},d})$, $p \in \mathcal{P}$.

The forecasted score vectors are mapped back to the functional domain by back-projection onto the retained eigenfunctions and then evaluated on the original observation grid. Although the functional observations are constructed from overlapping windows, this affects primarily the temporal dependence among curves rather than the FPCA machinery itself. Under standard regularity conditions, including consistent smoothing and weak dependence of the induced FTS, the estimators of the mean function, covariance kernel, and leading eigencomponents are consistent, see, for example [Bosq \(2000\)](#), [Horváth & Kokoszka \(2012\)](#), [Hörmann & Kokoszka \(2010\)](#).

3.3 Uncertainty Quantification for OLFTSA

We derive the uncertainty quantification procedure for OLFTSA, adapting the sequential conformal prediction framework of [Xu et al. \(2024\)](#). Recall that we constructed FTS using an overlapping rolling-window scheme, as illustrated in [Figure 2](#). For notational simplicity, we suppress the subscript p and define the actual forecast vector for d -th patch as $\hat{y}_d = (\hat{y}_d(t_{n'+1}), \dots, \hat{y}_d(t_n))^\top$, and the corresponding true values as $y_d = (y_d(t_{n'+1}), \dots, y_d(t_n))^\top$. We aim to construct a prediction region \mathcal{C}_d^α for each patch $d \geq D + 1$, conditional on past observations and the current timestamps $t_d = t = \{t_i\}_{i=n'+1}^n$, for a specified significance level $\alpha \in [0, 1]$, with coverage guarantees: a weaker marginal coverage and/or a stronger conditional coverage ([Gibbs et al. 2025](#)). Under coverage guarantees, regions with small volume provide more informative uncertainty quantification.

Assume that the forecasting model is trained. We use the first D patches as a calibration set, we compute residual vectors, $\hat{\varepsilon}_d = y_d - \hat{y}_d \in \mathfrak{R}^{n-n'}$, $d = 1, \dots, D$, and their empirical mean $\bar{\varepsilon} = \frac{1}{D} \sum_{d=1}^D \hat{\varepsilon}_d$. Let the sample covariance be $\tilde{\Sigma}_D = \frac{1}{D} \sum_{d=1}^D (\hat{\varepsilon}_d - \bar{\varepsilon})(\hat{\varepsilon}_d - \bar{\varepsilon})^\top$. In moderate- to high-dimensional settings, $\tilde{\Sigma}_D$ can be ill-conditioned. We apply entrywise thresholding to encourage sparsity (Kim et al. 2023): $\hat{\Sigma}_D = [\tilde{\sigma}_{j,k} \mathbb{1}(|\tilde{\sigma}_{j,k}| > \tau)]_{1 \leq j, k \leq n-n'}$, where $\tilde{\sigma}_{j,k}$ are the elements of $\tilde{\Sigma}_D$ and $\tau > 0$ is a tuning parameter. We use a Mahalanobis-type quadratic form as the nonconformity score. For any realization y for patch d , define

$$\hat{e}_d(y) = (y - \hat{y}_d - \bar{\varepsilon})^\top \hat{\Sigma}_D^{-1} (y - \hat{y}_d - \bar{\varepsilon}) \in \mathfrak{R}.$$

In particular, the realized calibration scores are $\hat{e}_d := \hat{e}_d(y_d)$ for $d = 1, \dots, D$, and we denote the score sequence by $\mathcal{E}_D = \{\hat{e}_d\}_{d=1}^D$. Because of the inherent dependency among the original data $\{y_d\}_{d=1}^D$, the scores in \mathcal{E}_D are not exchangeable. Instead of using the empirical $(1 - \alpha)$ -quantile of \mathcal{E}_D , we estimate an adaptive quantile of the score process using the sequential conformal quantile regression approach of Xu et al. (2024). See also the quantile random forests construction in Xu & Xie (2023). Concretely, let $\hat{Q}_d(\alpha)$ denote the fitted estimator of the α -quantile of \hat{e}_d , optionally conditional on predictors such as t_d or other available covariates. We then define the ellipsoidal prediction region for patch $d \geq D + 1$ as $\mathcal{C}_d^\alpha = \{y : \hat{Q}_d(\hat{\beta}) \leq \hat{e}(y) \leq \hat{Q}_d(1 - \alpha + \hat{\beta})\}$, where

$$\hat{\beta} = \arg \min_{\beta \in [0, \alpha]} \left\{ \hat{Q}_d(1 - \alpha + \beta)^\top \hat{\Sigma}_D^{-1} \hat{Q}_d(1 - \alpha + \beta) - \hat{Q}_d(\beta)^\top \hat{\Sigma}_D^{-1} \hat{Q}_d(\beta) \right\}.$$

The resulting set is an ellipsoid centered at $\hat{y}_d + \bar{\varepsilon}$ with shape determined by $\hat{\Sigma}_D^{-1}$. The full sequential calibration algorithm is given in Xu et al. (2024).

We now establish an asymptotic conditional coverage bound for the proposed conformal prediction region under dependent forecast errors. Let the true noise vector be ε_d with covariance matrix Σ , and define the theoretical score $e_d = \varepsilon_d^\top \Sigma^{-1} \varepsilon_d$. Relaxing the standard assumption of $\{\varepsilon_d\}_{d=1}^{D+1}$ being i.i.d., we assume that the sequence is stationary and strong mixing. Under Assumptions 1-5, we establish asymptotic conditional coverage validity of our procedure, accounting for estimation error in the noise covariance matrix; see Section A in the Online Supplementary Materials for details.

Assumption 1 (Stationarity and Strong Mixing). *The error sequence $\{\varepsilon_d\}_{d=1}^{D+1}$ is stationary and strong mixing (or α -mixing) with mixing coefficients satisfying $\sum_{l>0} \alpha_l < M$ for*

some constant $M < \infty$, where $\alpha_l = \sup_{d \in \mathbb{N}} \sup_{\mathcal{A} \in \mathcal{F}_1^d, \mathcal{B} \in \mathcal{F}_{d+l}^\infty} |P(\mathcal{A} \cap \mathcal{B}) - P(\mathcal{A})P(\mathcal{B})|$ and \mathcal{F}_a^b denotes the σ -algebra generated by $\{\varepsilon_a, \dots, \varepsilon_b\}$.

Stationarity implies that for any $j \geq 1$, integers d_1, \dots, d_j , and lag l , the joint distribution of $(\varepsilon_{d_1}, \dots, \varepsilon_{d_j})$ is identical to that of $(\varepsilon_{d_1+l}, \dots, \varepsilon_{d_j+l})$. The strong mixing condition requires that the coefficients α_l converge to zero as $l \rightarrow \infty$.

Assumption 2 (Lipschitz Continuity). *The cumulative distribution function of the true nonconformity score, denoted by $F_e(x) = P(e < x)$, is Lipschitz continuous with constant $L_{D+1} > 0$, that is, $F_e(x_1) - F_e(x_2) \leq L_{D+1}|x_1 - x_2|$ for all $x_1, x_2 \in \mathfrak{X}$.*

Assumption 3 (Prediction Error Bound). *There exists a sequence $\{\delta_D\}_{D \geq 1}$ such that $\frac{1}{D} \sum_{d=1}^D \|\hat{\varepsilon}_d - \varepsilon_d\|^2 \leq \delta_D^2$ and $\|\hat{\varepsilon}_{D+1} - \varepsilon_{D+1}\| \leq \delta_D$.*

This assumption bounds the aggregate prediction error. For consistent estimators, δ_D typically converges to zero as $D \rightarrow \infty$.

Assumption 4 (Covariance Regularity). *There exists a constant $\lambda > 0$ such that $\|\Sigma\| \geq \lambda$ and $\|\hat{\Sigma}_D\| \geq \lambda$, where $\|\cdot\|$ denotes the spectral norm.*

This condition ensures that both the true and estimated covariance matrices remain strictly positive definite, preventing singularity issues in the score computation.

Assumption 5 (Weak Dependence and Moment Conditions). *The sequence satisfies a short-range weak dependence condition. Specifically, for some $\omega > 0$,*

$$\Theta_{j,\omega} = \max_{n-n'+1 \leq i \leq n} \sum_{d=j}^{\infty} (E|\hat{\varepsilon}_{d,i} - \varepsilon_{d,i}|^\omega)^{1/\omega} < \infty.$$

Assume there exist $\omega > 4$ and positive constants c_1 and c_2 such that $\Theta_{j,\omega} \leq c_2 j^{-c_1}$ for all $j \geq 1$. For tail behavior, assume there exist positive constants c_3, c_4, c_5 such that $\max_{n-n'+1 \leq i \leq n} E|\varepsilon_{d,i}|^\omega < c_3$, $\max_{1 \leq d \leq D+1} |\varepsilon_d| \leq \sqrt{c_4 \omega}$ almost surely, and $\text{Var}[|\varepsilon_d|^2] \leq c_5 \omega$.

Theorem 1. *Under Assumptions 1–5, for any training sample size D and confidence level $\alpha \in (0, 1)$, the conditional coverage of uncertainty interval \mathcal{C}_{D+1}^α satisfies*

$$\begin{aligned} & |P(y_{D+1} \in \mathcal{C}_{D+1}^\alpha | t_{D+1}) - (1 - \alpha)| \\ & \leq \frac{12M^{1/3}(\log D)^{2/3}}{(2D)^{1/3}} + 4(L_{D+1}G(D, \tau) + 2L_{D+1} + 1)G(D, \tau), \end{aligned}$$

where

$$\begin{aligned}
G(D, \tau) &= \left\{ \frac{\delta_D^2}{\lambda} + \frac{C_1}{\lambda^2 \delta} (c_4 \omega + \sqrt{\frac{c_5 \omega}{D \delta}}) A(D, \tau) \right\}^{1/2}, \\
A(D, \tau) &= \left(\sum_{j,k=1}^{n-n'} \min(\tau^2, \sigma_{jk}^2) \right) + (n - n')^2 \min \left(\frac{1}{D}, \frac{\tau^{2-\omega/2}}{D^{\omega/4}}, H(\tau) \right),
\end{aligned} \tag{1}$$

and

$$H(\tau) = \begin{cases} \frac{\tau^{2-\omega/2}}{D^{\omega/2-1}} + C_2 \left(\frac{1}{D} + \tau^2 \right) e^{-D\tau^2}, & \text{if } c_2 > 1/2 - 2/\omega, \\ \frac{\tau^{2-\omega/2} (\log D)^{1+\omega/2}}{D^{\omega/2-1}} + C_2 \left(\frac{(\log D)^2}{D} + \tau^2 \right) e^{-\frac{D\tau^2}{(\log D)^2}}, & \text{if } c_2 = 1/2 - 2/\omega, \\ \frac{\tau^{2-\omega/2}}{D^{\omega/2(c_2+1/2)}} + C_2 \left(\frac{1}{D^{c_2}} + \tau^2 \right) e^{-D^{c_2}\tau^2}, & \text{if } c_2 < 1/2 - 2/\omega, \end{cases}$$

with $\tilde{c}_2 = (3 + c_2 \omega)/(1 + \omega/2)$. Here, C_1 and C_2 are constants independent of τ , D , and ω .

Remark 1. According to [Chen et al. \(2013\)](#), if the truncation parameter τ is chosen to be of order $D^{-1/2}$, then $A(D, \tau) = O(D^{-1})$. Consequently, $G(D, \tau) = O(D^{-1/2})$. The convergence rate of the coverage bound is therefore dominated by the first term, yielding $\frac{12M^{1/3}(\log D)^{2/3}}{(2D)^{1/3}} = O(D^{-1/3})$, which is consistent with the rate established in [Xu et al. \(2024\)](#).

3.4 Simulation Studies

In this section, we evaluate the proposed OLFTSA method for multivariate functional forecasting and uncertainty quantification. Synthetic data are generated following the process in [Trinka et al. \(2023\)](#), adapted for continuous FTS under rolling-window segmentation. This enables direct comparison with FSSA ([Trinka et al. 2023](#)) using the residual bootstrap for uncertainty quantification. We evaluate forecast accuracy via root mean square error (RMSE) and mean absolute error (MAE), and conformal coverage validity via empirical coverage probability (ECP) and mean interval width (MIW) at the nominal level 0.95.

The univariate continuous underlying process $z(s)$ is simulated over a global time domain $s \in [0, T]$ with $T = 100$, discretized at $N = \tilde{D}n$ equally spaced points $\{s_i\}_{i=1}^N$. Here, n denotes the length of each segmented curve; larger n yields finer temporal cadence, and larger \tilde{D} increases total number of patches to access asymptotic coverage. The underlying process is decomposed as $z(s) = m(s) + h(s)$, where $m(s)$ is the mean trend given by $m(s) = \nu s + \exp(\tilde{s}^2) \cos(2\pi\omega s) + \cos(4\pi\tilde{s}) \sin(2\pi\omega s)$ with drift rate $\nu = 0.02$, frequency $\omega = 0.2$, and local daily cycle $\tilde{s} = s \pmod{1}$. The term $h(s)$ is a stochastic component

constructed via a basis expansion with time-varying coefficients, $h(s) = \sum_{j=1}^J \zeta_j(s) \psi_j(\tilde{s})$, where $\{\psi_j(\cdot)\}_{j=1}^J$ are fixed Fourier basis functions on the local domain with $J = 5$, ensuring a smooth functional structure. The latent coefficients $\zeta(s) = (\zeta_1(s), \dots, \zeta_J(s))^\top$ follow a vector autoregressive process of order 1: $\zeta(s) = A\zeta(s - \Delta_s) + \eta(s)$, $\eta(s) \sim N(0, 0.05^2 \mathbf{I}_J)$, where Δ_s is the discretization step. To simulate strong day-to-day autocorrelation (≈ 0.8), the transition matrix $A \in \mathfrak{R}^{J \times J}$ is chosen to be diagonal with decreasing diagonal entries. One sample trajectory is shown in Figure B.3 in the Online Supplementary Materials.

To transform $z(s)$ into FTS observations $\{y_d(t_i), i = 1, \dots, n\}_{d=1}^D$ as described in Section 3.1, we employ a rolling-window segmentation scheme. The d -th observed curve with measurement error is given by $y_d(t_i) = z(s_{(d-1)n(1-\gamma)+i}) + \epsilon_{d,i}$, where $\epsilon_{d,i} \sim N(0, 0.05^2)$. The overlap ratio is $\gamma = n'/n \in [0, 1)$, where n' is the number of shared points between consecutive curves; $\gamma = 0$ corresponds to a standard non-overlapping segmentation.

We consider $\tilde{D} \in \{150, 300\}$, $n \in \{100, 300, 500\}$ and $\gamma \in \{0, 0.4, 0.6, 0.8\}$. For each configuration, we perform a 60%/40% split for training and testing. We compare the proposed OLFSTA method, which employs quantile random forests for multivariate conformal prediction, against the FSSA method equipped with residual-based bootstrap resampling (Trinka et al. 2023). The results are averaged over 10 replications. Figure 3 summarizes the results for the larger setting $\tilde{D} = 300$. Similar patterns hold for $\tilde{D} = 150$; the full numerical results for both settings are reported in Tables B.3 B.2 in the Online Supplementary Materials. The FSSA method slightly outperforms OLFSTA for point estimates under the non-overlapping setting for smaller curve lengths (e.g., $n \in \{100, 300\}$), which aligns with the findings in Trinka et al. (2023). However, the benefits of the overlapping scheme are evident: as the overlap ratio γ increases, both RMSE and MAE decrease, and OLFSTA significantly outperforms FSSA at higher overlap levels (e.g., $\gamma \geq 0.4$). For uncertainty quantification, the OLFSTA conformal prediction achieves coverage probabilities close to the nominal level across all settings, whereas the FSSA's residual-based bootstrap suffers from severe undercoverage and wider interval widths. Furthermore, increasing the overlap ratio for OLFSTA leads to sharper inference with narrower interval widths without compromising coverage. As the number of patches \tilde{D} increases, the empirical coverage probabilities of OLFSTA get close to the nominal level, demonstrating the asymptotic validity of the procedure. Finally, the proposed OLFSTA is computationally superior, requiring

significantly less time than the FSSA approach.

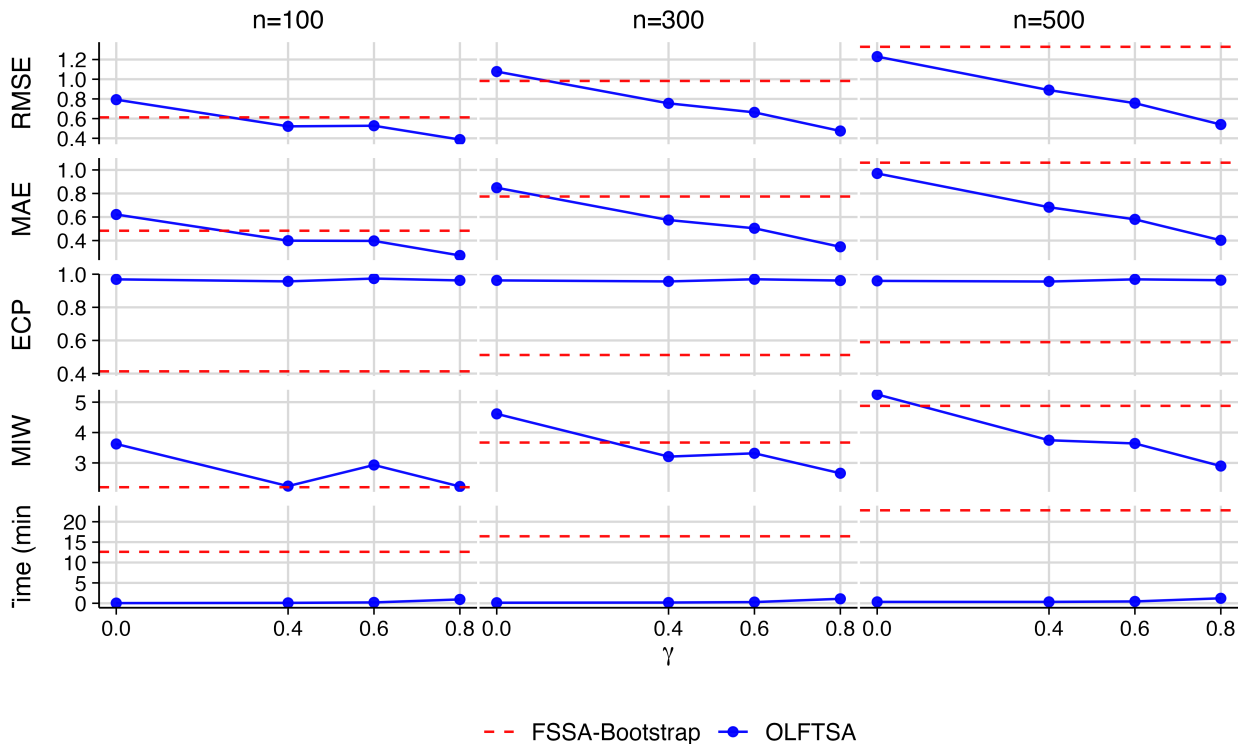


Figure 3: Simulation results for $\tilde{D} = 300$ comparing the proposed OLF-TSA method under varying overlap ratios γ with FSSA-Bootstrap for three curve lengths, $n = 100, 300,$ and 500 . Rows display point forecast accuracy (RMSE and MAE), uncertainty quantification performance at nominal coverage level 0.95 (ECP and MIW), and computational time in minutes. Blue solid lines with points represent OLF-TSA, while red dashed horizontal lines represent FSSA-Bootstrap. Results are averaged over 10 replications.

4 Application on Geomagnetic Indices Data

We apply the OLF-TSA framework to the geomagnetic index data described in Section 2. Data is split into training and testing sets for a rigorous out-of-sample evaluation. Data spanning January 1, 1995 through December 31, 2019 are used for model training, covering solar cycles 23 and 24, while data from January 1, 2020 through 2025 in solar cycle 25 serve as the held-out test set. Forecasting performance is evaluated using three standard metrics: RMSE and MAE to quantify the magnitude of forecast errors, and the Pearson correlation coefficient (R) to assess phase agreement between predicted and observed indices.

We assess the model’s ability to forecast the temporal evolution of the magnetosphere-ionosphere system under varying solar wind driving conditions. We benchmark the proposed OLFTSA framework against the long short-term memory (LSTM) network, a standard deep learning baseline in space weather forecasting (Tan et al. 2018, Polozov 2023, Nair et al. 2023), as well as the CHRONOS time series foundation model (Ansari et al. 2024). For the LSTM baseline, we adopt a stacked encoder-decoder architecture tailored for multivariate sequence-to-sequence forecasting, with min-max normalization applied to all input channels to improve training stability and convergence. The encoder comprises two LSTM layers with sequence return enabled to preserve temporal structure, followed by 10% dropout for regularization, while decoding proceeds through a dense layer with ReLU activation and a final linear layer projecting to the forecast horizon. For CHRONOS, we employ the base (smallest) variant without multivariate extensions or covariate incorporation (see (Ansari et al. 2025) for an enhanced version), reflecting a conservative design choice motivated by the prohibitive sequence lengths associated with multi-hour, high-resolution geomagnetic forecasts. This setup prioritizes computational efficiency, yet still provides a stringent baseline and highlights the potential benefits of scaling to larger foundation models as computational resources increase. Forecasting results are stratified by horizon (6-hour and 24-hour ahead), patch duration (window length), and geomagnetic index to disentangle performance across distinct magnetospheric current systems.

Table 1: Six-hour ahead forecast performance comparison.

Index	OLFTSA			LSTM			CHRONOS		
	RMSE	MAE	R	RMSE	MAE	R	RMSE	MAE	R
Kp	0.8360	0.6330	0.7665	1.0123	0.8442	0.7264	0.9484	0.7099	0.6933
Dst	8.4104	5.0397	0.9070	13.3263	10.0410	0.8310	10.1035	5.8273	0.8629
SYM-H	8.8909	5.2990	0.9010	12.5482	9.4569	0.8474	10.7060	6.0783	0.8538
SMR	8.9326	5.0798	0.8858	13.8956	10.8873	0.8294	10.5271	5.5673	0.8403
SME	162.9377	106.1887	0.6525	222.0116	190.3414	0.5874	180.7999	107.2291	0.5774

In 6-hour forecasts, the OLFTSA attains lower RMSE and MAE and higher correlations than both LSTM and CHRONOS for all five indices (Table 1). For the Dst index, which is central to storm-time ring-current monitoring, OLFTSA with a 48-hour window length

(corresponding to an overlap ratio of $(48 - 6)/48 = 0.8750$) attains an RMSE of 8.4104 nT, compared with 13.3263 for LSTM and 10.1035 for CHRONOS. Figure 4 illustrates the 6-hour ahead forecasts during an intense geomagnetic storm event in solar cycle 25. The event features a rapid intensification where index values plummet to approximately -400 nT. OLFTSA captures the sharp main-phase drop to nearly -400 nT and the subsequent recovery of the ring current with a relatively smooth trajectory. The LSTM model exhibits pronounced high-frequency instability, which is particularly noticeable in the high-resolution SMR forecasts. The auroral electrojet index SME, characterized by strong stochasticity and bursty auroral dynamics, remains the most challenging target; in this case, OLFTSA still achieves the highest correlation of 0.6525, compared with 0.5874 for LSTM and 0.5774 for CHRONOS, showing the benefit of functional representation in high-frequency variability.

Extending the forecast horizon to 24 hours introduces greater uncertainty and yields performance degradation across all models. For the planetary Kp index, OLFTSA with a 72-hour window length (corresponding to an overlap ratio of $(72 - 24)/72 = 0.6667$) maintains a correlation of 0.5899, whereas CHRONOS and LSTM drop to 0.4909 and 0.4630, respectively. For Dst and SYM-H, forecasting errors naturally increase at 24 hours, but the functional approach still yields higher correlations (above 0.75) than both deep-learning baselines, indicating better retention of large-scale storm morphology at longer lead times (Table C.2 in Online Supplementary Material). Forecasting SME at a 24-hour horizon is expected to be particularly challenging because auroral substorms typically have much shorter life cycles and are often triggered by solar wind disturbances occurring only tens of minutes in advance. This inherently limits predictability at such long lead times. Figure 5 shows the forecasts for a highly active SME interval in March 2021, where it exhibited marked stochasticity and rapid excursions beyond 2000 nT. OLFTSA achieves higher correlations than LSTM and CHRONOS and reproduces the temporal structure and envelope of activity more closely, although some extreme peaks are underestimated. Once functional features are extracted, forecasting reduces to a standard multivariate time series prediction, which is faster than the transformer-based CHRONOS model.

The proposed model provides improved forecasting accuracy while giving predictive uncertainty for each geomagnetic index with reduced computational cost. For the 6-hour ahead

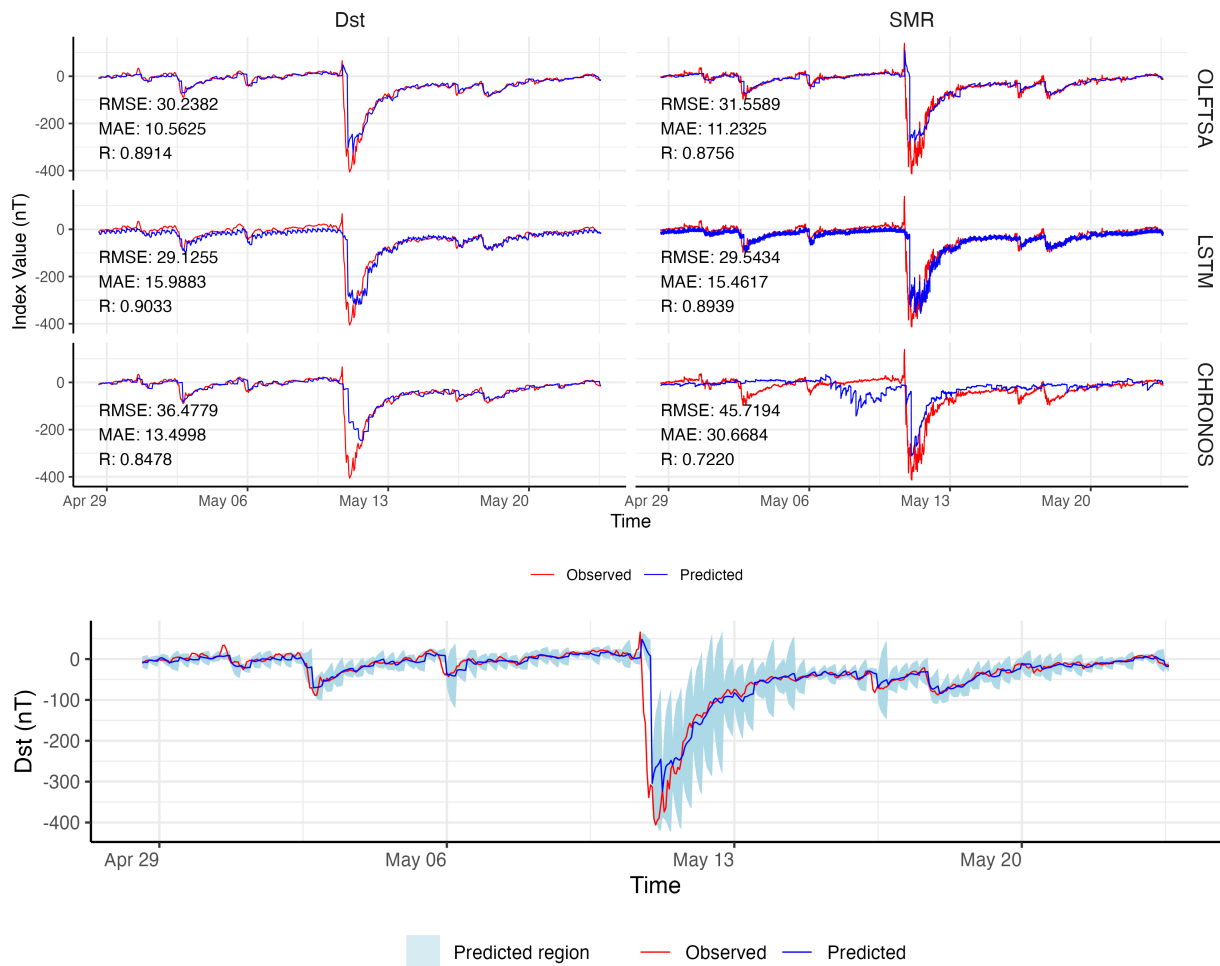


Figure 4: Six-hour ahead forecasting performance for Dst and SMR indices during an intense geomagnetic storm event (May 2024). The top panel compares the observed (red) and predicted (blue) values from OLFTSA (top), LSTM (middle), and CHRONOS (bottom). The bottom panel shows the prediction intervals of Dst given by the conformal method.

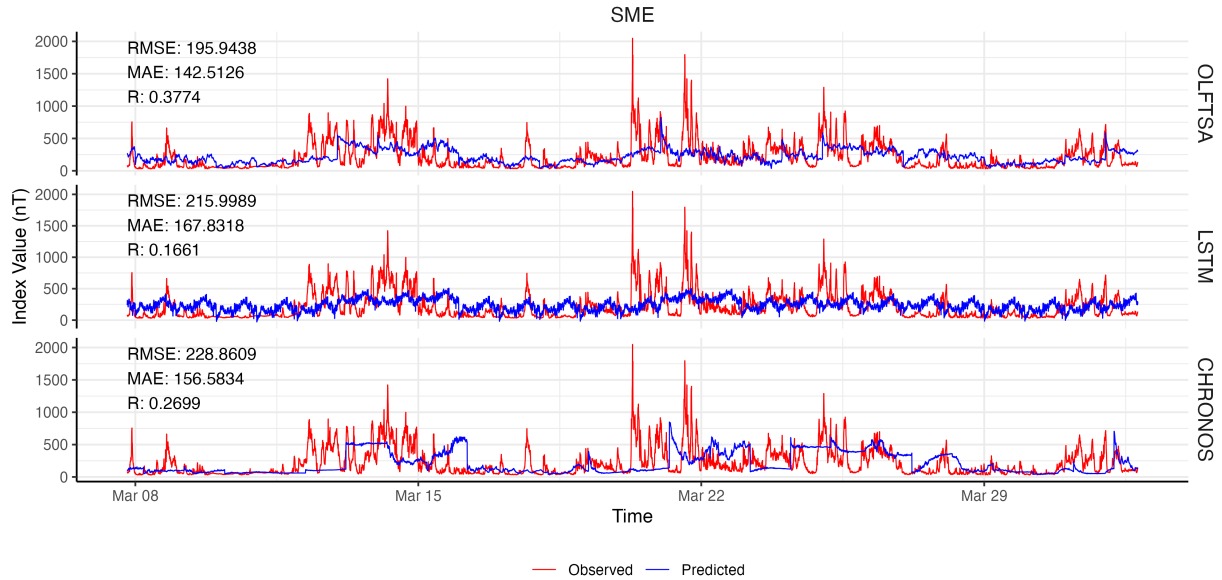


Figure 5: Twenty-four-hour ahead forecasting for SME during a highly active time (Mar 2021) with OLFTSA, LSTM and CHRONOS.

forecasts, where the number of input patches is larger, the Dst index achieves an ECP of 0.9236 and an MIW of 28.0710 nT, as illustrated in Figure 4. When the forecasting horizon extends to 24 hours, the ECP for Dst decreases to 0.8918 with an MIW of 56.6433 nT, while the SYM-H index attains an ECP of 0.8968 and an MIW of 58.8388 nT.

For 24-hour ahead forecasting, each Kp prediction step under OLFTSA requires on average 0.9347 seconds, while SYM-H predictions, due to their higher temporal resolution, require 15.4439 seconds on average. The CHRONOS foundation model requires on average 1.6118 seconds for Kp, 2.3443 seconds for Dst, and 20.6746 seconds for SYM-H. After extracting functional PCs from the training data, OLFTSA forecasting reduces to multivariate time series prediction (see Section 3), which is not time-consuming. Figure 6 compares computational costs across low-resolution Kp, medium-resolution Dst, and high-resolution SYM-H. Training the multivariate forecasting model utilizes all data from 1995 through the current time. Prediction times therefore increase slightly as the forecast horizon is extended.

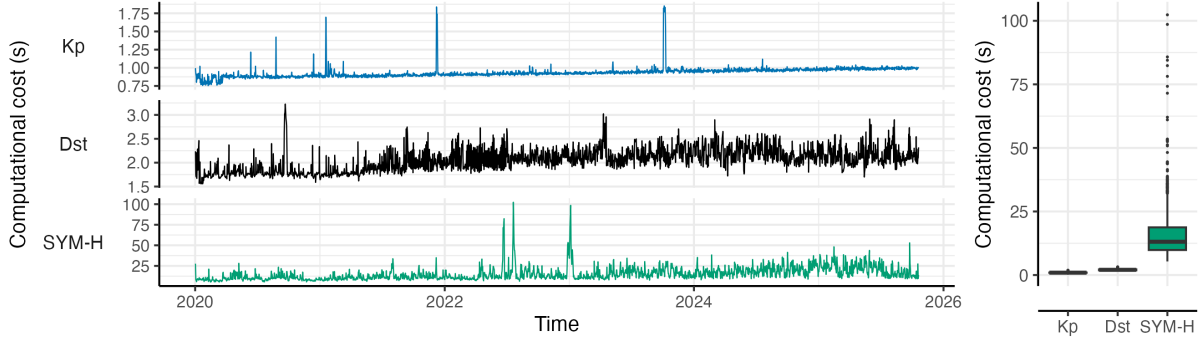


Figure 6: Computational costs for 24-hour ahead forecasting of Kp (low-resolution), Dst (medium-resolution), and SYM-H (high-resolution).

5 Conclusion

This paper introduces an overlapping FTS analysis framework integrated with conformal prediction for multivariate forecasting of geomagnetic indices. The methodology combines extended temporal windowing, FPCA, and multivariate time series modeling to accommodate heterogeneous indices in space weather prediction.

The overlapping rolling-window approach improves estimation stability over non-overlapping schemes. Representing 48–72 hour patches in functional form helps maintain temporal continuity, while FPCA-based dimensionality reduction facilitates joint forecasting of Kp, Dst, SYM-H, SME, and SMR indices using solar wind parameters. In the applications considered here, the method attains lower forecast errors and higher correlations than LSTM and CHRONOS benchmarks, particularly at 6-hour horizons, with comparable behavior at 24 hours. Extending window lengths with increased overlap ratios appears beneficial in these experiments, although longer windows require retaining more functional PCs and therefore increase computational costs in the multivariate forecasting step.

The adapted conformal prediction procedure provides distribution-free coverage guarantee theoretically, and produce empirical coverage probabilities close to the nominal 95% level. This offers a robust mechanism for uncertainty quantification that can be reliably adopted in operational settings. The OLFTSA framework is also relatively efficient computationally, with per-step predictions requiring on the order of seconds rather than several minutes

typically associated with the deep-learning baselines considered here.

Data and Code Availability

The data and code are available at <https://doi.org/10.5281/zenodo.20274712>.

Acknowledgments

Chen’s work is supported by funds from the the NASA Space Weather Center of Excellence program under award No. 80NSSC23M0191 and No. 80NSSC23M0192.

References

- Ansari, A. F., Shchur, O., Küken, J., Auer, A., Han, B., Mercado, P., Rangapuram, S. S., Shen, H., Stella, L., Zhang, X., Goswami, M., Kapoor, S., Maddix, D. C., Gueron, P., Hu, T., Yin, J., Erickson, N., Desai, P. M., Wang, H., Rangwala, H., Karypis, G., Wang, Y. & Bohlke-Schneider, M. (2025), ‘Chronos-2: From univariate to universal forecasting’.
URL: <https://arxiv.org/abs/2510.15821>
- Ansari, A. F., Stella, L., Turkmen, C., Zhang, X., Mercado, P., Shen, H., Shchur, O., Rangapuram, S. S., Arango, S. P., Kapoor, S., Zschiegner, J., Maddix, D. C., Wang, H., Mahoney, M. W., Torkkola, K., Wilson, A. G., Bohlke-Schneider, M. & Wang, Y. (2024), ‘Chronos: Learning the language of time series’.
URL: <https://arxiv.org/abs/2403.07815>
- Antoniadis, A., Paparoditis, E. & Sapatinas, T. (2006a), ‘A functional wavelet–kernel approach for time series prediction’, *Journal of the Royal Statistical Society Series B: Statistical Methodology* **68**(5), 837–857.
URL: <https://doi.org/10.1111/j.1467-9868.2006.00569.x>
- Antoniadis, A., Paparoditis, E. & Sapatinas, T. (2006b), ‘A functional wavelet–kernel approach for time series prediction’, *Journal of the Royal Statistical Society Series B: Statistical Methodology* **68**(5), 837–857.
URL: <https://doi.org/10.1111/j.1467-9868.2006.00569.x>

- Ash, R. B. & Gardner, M. F. (1975), *Topics in Stochastic Processes*, Probability and Mathematical Statistics: A Series of Monographs and Textbooks, Academic Press.
URL: <https://www.sciencedirect.com/science/article/pii/B9780120652709500147>
- Aue, A., Norinho, D. D. & Hörmann, S. (2015), ‘On the prediction of stationary functional time series’, *Journal of the American Statistical Association* **110**(509), 378–392.
URL: <https://doi.org/10.1080/01621459.2014.909317>
- Ayala Solares, J. R., Wei, H.-L., Boynton, R. J., Walker, S. N. & Billings, S. A. (2016), ‘Modeling and prediction of global magnetic disturbance in near-Earth space: A case study for Kp index using NARX models’, *Space Weather* **14**(10), 899–916.
URL: <https://agupubs.onlinelibrary.wiley.com/doi/abs/10.1002/2016SW001463>
- Bokde, N., Asencio-Cortés, G., Martínez-Álvarez, F. & Kulat, K. (2017), ‘PSF: Introduction to R package for pattern sequence based forecasting algorithm’, *The R Journal* **9**, 324–333. <https://doi.org/10.32614/RJ-2017-021>.
- Bosq, D. (2000), *Linear Processes in Function Spaces: Theory and Applications*, Lecture Notes in Statistics, Springer New York.
- Camporeale, E. (2019), ‘The challenge of machine learning in space weather: Nowcasting and forecasting’, *Space Weather* **17**(8), 1166–1207.
URL: <https://agupubs.onlinelibrary.wiley.com/doi/abs/10.1029/2018SW002061>
- Chandorkar, M., Camporeale, E. & Wing, S. (2017), ‘Probabilistic forecasting of the disturbance storm time index: An autoregressive gaussian process approach’, *Space Weather* **15**(8), 1004–1019.
- Chen, H., Toth, G., Chen, Y., Zou, S., Huang, Z. & Huan, X. (2025), ‘Geodgp: One-hour ahead global probabilistic geomagnetic perturbation forecasting using deep gaussian process’, *Space Weather* **23**(6), e2024SW004301.
- Chen, X., Xu, M. & Wu, W. B. (2013), ‘Covariance and precision matrix estimation for high-dimensional time series’, *The Annals of Statistics* **41**(6).
- Chen, Y., Manchester, W., Jin, M. & Pevtsov, A. (2024), ‘Solar imaging data analytics:

- A selective overview of challenges and opportunities’, *Statistics and Data Science in Imaging* **1**(1), 2391688.
- Erbas, B., Hyndman, R. J. & Gertig, D. M. (2007), ‘Forecasting age-specific breast cancer mortality using functional data models’, *Statistics in Medicine* **26**(2), 458–470.
URL: <https://onlinelibrary.wiley.com/doi/abs/10.1002/sim.2306>
- Fung, S. F. & Shao, X. (2008), ‘Specification of multiple geomagnetic responses to variable solar wind and IMF input’, *Annales Geophysicae* **26**(3), 639–652.
URL: <https://angeo.copernicus.org/articles/26/639/2008/>
- Gertheiss, J., Rügamer, D., Liew, B. X. & Greven, S. (2024), ‘Functional data analysis: An introduction and recent developments’, *Biometrical Journal* **66**(7), e202300363.
- Gibbs, I., Cherian, J. J. & Candès, E. J. (2025), ‘Conformal prediction with conditional guarantees’, *Journal of the Royal Statistical Society Series B: Statistical Methodology* **87**(4), 1100–1126.
- Gohberg, I., Goldberg, S. & Kaashoek, M. (2012), *Basic Classes of Linear Operators*, Mathematics and Statistics, Birkhäuser Basel.
- Goldsmith, J., Greven, S. & Crainiceanu, C. (2013), ‘Corrected confidence bands for functional data using principal components’, *Biometrics* **69**(1), 41–51.
URL: <https://onlinelibrary.wiley.com/doi/abs/10.1111/j.1541-0420.2012.01808.x>
- González, J. P., San Roque, A. M. S. M. & Perez, E. A. (2017), ‘Forecasting functional time series with a new Hilbertian ARMAX model: Application to electricity price forecasting’, *IEEE Transactions on Power Systems* **33**(1), 545–556.
- Hagbin, H., Najibi, S. M., Mahmoudvand, R., Trinka, J. & Maadooliat, M. (2021), ‘Functional singular spectrum analysis’, *Stat* **10**(1), e330.
URL: <https://onlinelibrary.wiley.com/doi/abs/10.1002/sta4.330>
- Hörmann, S. & Kokoszka, P. (2010), ‘Weakly dependent functional data’, *The Annals of Statistics* **38**(3), 1845 – 1884.
- Horváth, L. & Kokoszka, P. (2012), *Inference for Functional Data with Applications*, Vol. 200 of *Springer Series in Statistics*, Springer Science & Business Media.

- Hsing, T. & Eubank, R. L. (2015), *Theoretical foundations of functional data analysis, with an introduction to linear operators*, Vol. 997 of *Wiley Series in Probability and Statistics*, Wiley Online Library.
- Hu, A., Camporeale, E. & Swiger, B. (2023), ‘Multi-hour-ahead dst index prediction using multi-fidelity boosted neural networks’, *Space Weather* **21**(4), e2022SW003286.
- Hyndman, R. J. & Ullah, M. S. (2007), ‘Robust forecasting of mortality and fertility rates: A functional data approach’, *Computational Statistics & Data Analysis* **51**(10), 4942–4956.
- Long, D., Chen, Y., Toth, G., Zou, S., Pulkkinen, T., Ren, J., Camporeale, E. & Gombosi, T. (2022), ‘New findings from explainable SYM-H forecasting using gradient boosting machines’, *Space Weather* **20**(8), e2021SW002928.
URL: <https://agupubs.onlinelibrary.wiley.com/doi/abs/10.1029/2021SW002928>
- Long, D., McAnear, M., Qu, Y., Zou, S., Toth, G. & Chen, Y. (2024), ‘Sparse variational contaminated noise gaussian process regression with applications in geomagnetic perturbations forecasting’, *Data Science in Science* **3**(1), 2383281.
- Jolliffe, I. (2002), *Principal Component Analysis*, Springer Series in Statistics, Springer.
- Kaiser, H. F. (1958), ‘The varimax criterion for analytic rotation in factor analysis’, *Psychometrika* **23**(3), 187–200.
- Khabarova, O. & Price, C. (2024), ‘Importance and challenges of geomagnetic storm forecasting’, *Frontiers in Astronomy and Space Sciences* **11**.
URL: <https://www.frontiersin.org/journals/astronomy-and-space-sciences/articles/10.3389/fspas.2024.1493917>
- Kim, R., Pourahmadi, M. & Garcia, T. P. (2023), ‘Positive-definite thresholding estimators of covariance matrices with zeros’, *Journal of Multivariate Analysis* **197**, 105186.
URL: <https://www.sciencedirect.com/science/article/pii/S0047259X23000325>
- Laperre, B., Amaya, J. & Lapenta, G. (2020), ‘Dynamic time warping as a new evaluation for dst forecast with machine learning’, *Frontiers in Astronomy and Space Sciences* **7**, 540918.

- Nair, M., Redmon, R., Young, L.-Y., Chulliat, A., Trotta, B., Chung, C., Lipstein, G. & Slavitt, I. (2023), ‘MagNet—a data-science competition to predict disturbance storm-time index (Dst) from solar wind data’, *Space Weather* **21**(10), e2023SW003514.
URL: <https://agupubs.onlinelibrary.wiley.com/doi/abs/10.1029/2023SW003514>
- Newell, P. T., Sotirelis, T., Liou, K., Meng, C.-I. & Rich, F. J. (2007), ‘A nearly universal solar wind-magnetosphere coupling function inferred from 10 magnetospheric state variables’, *Journal of Geophysical Research: Space Physics* **112**(A1).
URL: <https://agupubs.onlinelibrary.wiley.com/doi/abs/10.1029/2006JA012015>
- Park, W., Lee, J., Kim, K.-C., Lee, J., Park, K., Miyashita, Y., Sohn, J., Park, J., Kwak, Y.-S., Hwang, J. et al. (2021), ‘Operational dst index prediction model based on combination of artificial neural network and empirical model’, *Journal of Space Weather and Space Climate* **11**, 38.
- Polozov, Y. (2023), SME geomagnetic index data forecast based on wavelet transform and LSTM neural networks, in ‘International Conference Solar-terrestrial Relations and Physics of Earthquake Precursors’, Springer, pp. 186–196.
- Ramsay, J., Hooker, G. & Graves, S. (2009), *Functional Data Analysis with R and MATLAB*, Use R!, Springer New York.
- Ramsay, J. & Silverman, B. (2005), *Functional Data Analysis*, Springer Series in Statistics, Springer.
- Shang, H. L. (2013), ‘Functional time series approach for forecasting very short-term electricity demand’, *Journal of Applied Statistics* **40**(1), 152–168.
- Shang, H. L. (2019), ‘A robust functional time series forecasting method’, *Journal of Statistical Computation and Simulation* **89**(5), 795–814.
- Sokolova, O., Korovkin, N. & Hayakawa, M. (2021), *Geomagnetic Disturbances Impacts on Power Systems: Risk Analysis and Mitigation Strategies*, CRC Press.
- Tan, Y., Hu, Q., Wang, Z. & Zhong, Q. (2018), ‘Geomagnetic index Kp forecasting with LSTM’, *Space Weather* **16**(4), 406–416.

- Trinka, J., Haghbin, H., Lin Shang, H. & Maadooliat, M. (2023), ‘Functional time series forecasting: Functional singular spectrum analysis approaches’, *Stat* **12**(1), e621.
URL: <https://onlinelibrary.wiley.com/doi/abs/10.1002/sta4.621>
- Trinka, J., Haghbin, H. & Maadooliat, M. (2022), Multivariate functional singular spectrum analysis: A nonparametric approach for analyzing multivariate functional time series, *in* ‘Innovations in multivariate statistical modeling: Navigating theoretical and multidisciplinary domains’, Springer, pp. 187–221.
- Wang, J., Luo, B., Liu, S. & Shi, L. (2023), ‘A machine learning-based model for the next 3-day geomagnetic index (Kp) forecast’, *Frontiers in Astronomy and Space Sciences* **10**.
- Xu, C., Jiang, H. & Xie, Y. (2024), Conformal prediction for multi-dimensional time series by ellipsoidal sets, *in* ‘Proceedings of the 41st International Conference on Machine Learning’, Vol. 235 of *Proceedings of Machine Learning Research*, PMLR, pp. 55076–55099.
URL: <https://proceedings.mlr.press/v235/xu24m.html>
- Xu, C. & Xie, Y. (2023), Sequential predictive conformal inference for time series, *in* ‘Proceedings of the 40th International Conference on Machine Learning’, Vol. 202 of *Proceedings of Machine Learning Research*, PMLR, pp. 38707–38727.
URL: <https://proceedings.mlr.press/v202/xu23r.html>
- Xue, D., Wu, L., Xu, T., Wu, C.-L., Wang, Z. & He, Z. (2024), ‘Space weather effects on transportation systems: A review of current understanding and future outlook’, *Space Weather* **22**(12), e2024SW004055.
- Yao, F., Müller, H.-G. & Wang, J.-L. (2005), ‘Functional data analysis for sparse longitudinal data’, *Journal of the American Statistical Association* **100**(470), 577–590.
URL: <https://doi.org/10.1198/016214504000001745>
- Yu, Y., Tang, L., Ren, K., Chen, Z., Chen, S. & Shi, J. (2024), ‘Bayesian regression analysis for dependent data with an elliptical shape’, *Entropy* **26**(12).
URL: <https://www.mdpi.com/1099-4300/26/12/1072>

SUPPLEMENTARY MATERIALS

Stable Multivariate Functional Time Series Prediction for Major Geomagnetic Indices

A Proof of Theorem 1

We begin by recalling the necessary notation. The estimated prediction residual is defined as $\hat{\varepsilon}_d = y_d - \hat{y}_d \in \mathfrak{R}^{n-n'}$, and the scalar nonconformity score is given by $\hat{e}_d = \hat{\varepsilon}_d^T \hat{\Sigma}_D^{-1} \hat{\varepsilon}_d \in \mathfrak{R}$. The corresponding true noise vector is ε_d , with covariance Σ , yielding the theoretical score $e_d = \varepsilon_d^T \Sigma^{-1} \varepsilon_d$.

We define the empirical cumulative distribution functions (CDFs) for the estimated and true scores as $\hat{F}_{D+1}(x) = \frac{1}{D} \sum_{d=1}^D \mathbb{1}\{\hat{e}_d < x\}$ and $\tilde{F}_{D+1}(x) = \frac{1}{D} \sum_{d=1}^D \mathbb{1}\{e_d < x\}$, respectively. The CDF of the true nonconformity score is denoted by $F_e(x) = P(e < x)$. By the probability integral transform, $F_e(\cdot)$ is uniformly distributed on $[0, 1]$ with continuous and strictly increasing scores.

Proof. For any $\beta \in [0, \alpha]$, the deviation of the conditional coverage from the nominal level $1 - \alpha$ can be bounded as follows:

$$\begin{aligned}
 & \left| P(y_{D+1} \in \mathcal{C}_{D+1}^\alpha | t_{D+1}) - (1 - \alpha) \right| \\
 &= \left| P(\beta < \hat{F}_{D+1}(\hat{e}_{D+1}) < 1 - \alpha + \beta) - (1 - \alpha) \right| \\
 &= \left| P(\beta < \hat{F}_{D+1}(\hat{e}_{D+1}) < 1 - \alpha + \beta) - P(\beta < F_e(e_{D+1}) < 1 - \alpha + \beta) \right| \\
 &\leq \mathbb{E} \left| \mathbb{1}\{\beta < \hat{F}_{D+1}(\hat{e}_{D+1}) < 1 - \alpha + \beta\} - \mathbb{1}\{\beta < F_e(e_{D+1}) < 1 - \alpha + \beta\} \right| \\
 &\leq \mathbb{E} \left| \mathbb{1}\{\beta < \hat{F}_{D+1}(\hat{e}_{D+1})\} - \mathbb{1}\{\beta < F_e(e_{D+1})\} \right| \\
 &\quad + \mathbb{E} \left| \mathbb{1}\{\hat{F}_{D+1}(\hat{e}_{D+1}) < 1 - \alpha + \beta\} - \mathbb{1}\{F_e(e_{D+1}) < 1 - \alpha + \beta\} \right|. \tag{A.1}
 \end{aligned}$$

Using the inequality

$$\begin{aligned}
& \left| \mathbb{1}\{a \leq x \leq b\} - \mathbb{1}\{a \leq x' \leq b\} \right| \\
& \leq \left| \mathbb{1}\{a \leq x\} - \mathbb{1}\{a \leq x'\} \right| + \left| \mathbb{1}\{x \leq b\} - \mathbb{1}\{x' \leq b\} \right| \\
& \leq \mathbb{1}\{|a - x'| \leq |x - x'|\} + \mathbb{1}\{|b - x'| \leq |x - x'|\}
\end{aligned}$$

for any constants a, b and real-valued random variables x and x' , we can bound the right-hand side of (A.1) by

$$\begin{aligned}
& \mathbb{E} \left| \mathbb{1}\{\beta < \hat{F}_{D+1}(\hat{e}_{D+1})\} - \mathbb{1}\{\beta < F_e(e_{D+1})\} \right| \\
& \quad + \mathbb{E} \left| \mathbb{1}\{\hat{F}_{D+1}(\hat{e}_{D+1}) < 1 - \alpha + \beta\} - \mathbb{1}\{F_e(e_{D+1}) < 1 - \alpha + \beta\} \right| \\
& \leq \mathbb{E} \left[\mathbb{1}\left\{ \left| F_e(e_{D+1}) - \beta \right| \leq \left| \hat{F}_{D+1}(\hat{e}_{D+1}) - F_e(e_{D+1}) \right| \right\} \right] \\
& \quad + \mathbb{E} \left[\mathbb{1}\left\{ \left| F_e(e_{D+1}) - (1 - \alpha + \beta) \right| \leq \left| \hat{F}_{D+1}(\hat{e}_{D+1}) - F_e(e_{D+1}) \right| \right\} \right] \\
& = P \left(\left| F_e(e_{D+1}) - \beta \right| \leq \left| \hat{F}_{D+1}(\hat{e}_{D+1}) - F_e(e_{D+1}) \right| \right) \\
& \quad + P \left(\left| F_e(e_{D+1}) - (1 - \alpha + \beta) \right| \leq \left| \hat{F}_{D+1}(\hat{e}_{D+1}) - F_e(e_{D+1}) \right| \right). \tag{A.2}
\end{aligned}$$

Invoking Lemma C.11 of Xu et al. (2024) under Assumptions 1 and 2, define the event

$$\mathcal{A}_D = \left\{ \sup_x \left| \tilde{F}_{D+1}(x) - F_e(x) \right| \leq \frac{M^{1/3}(\log D)^{2/3}}{(2D)^{1/3}} \right\}.$$

Then $P(\mathcal{A}_D) > 1 - \frac{M^{1/3}(\log D)^{2/3}}{(2D)^{1/3}}$, and conditional on \mathcal{A}_D the same bound holds for the supremum distance.

For any constant $\gamma \in [0, 1]$, we can decompose the probability bound

$$\begin{aligned}
& P \left(\left| F_e(e_{D+1}) - \gamma \right| \leq \left| \hat{F}_{D+1}(\hat{e}_{D+1}) - F_e(e_{D+1}) \right| \right) \\
& \leq P \left(\left| F_e(e_{D+1}) - \gamma \right| \leq \left| \hat{F}_{D+1}(\hat{e}_{D+1}) - F_e(e_{D+1}) \right| \mid \mathcal{A}_D \right) + 1 - P(\mathcal{A}_D).
\end{aligned}$$

Applying the triangle inequality,

$$\begin{aligned}
& \left| \widehat{F}_{D+1}(\widehat{e}_{D+1}) - F_e(e_{D+1}) \right| \mathcal{A}_D \\
& \leq \left| \widehat{F}_{D+1}(\widehat{e}_{D+1}) - F_e(\widehat{e}_{D+1}) \right| + \left| F_e(\widehat{e}_{D+1}) - F_e(e_{D+1}) \right| \mathcal{A}_D \\
& \leq \sup_x \left| \widehat{F}_{D+1}(x) - \widetilde{F}_{D+1}(x) \right| \mathcal{A}_D + \sup_x \left| \widetilde{F}_{D+1}(x) - F_e(x) \right| \mathcal{A}_D + L_{D+1} |\widehat{e}_{D+1} - e_{D+1}|.
\end{aligned}$$

Substituting the bound on \mathcal{A}_D , we have

$$\begin{aligned}
& \left| \widehat{F}_{D+1}(\widehat{e}_{D+1}) - F_e(e_{D+1}) \right| \mathcal{A}_D \\
& \leq \sup_x \left| \widehat{F}_{D+1}(x) - \widetilde{F}_{D+1}(x) \right| \mathcal{A}_D + \frac{M^{1/3}(\log D)^{2/3}}{(2D)^{1/3}} + L_{D+1} |\widehat{e}_{D+1} - e_{D+1}|.
\end{aligned}$$

Using Lemmas A.2 and A.3, we have $|\widehat{e}_{D+1} - e_{D+1}| \leq G(D, \tau)^2$ and

$$\begin{aligned}
\sup_x \left| \widehat{F}_{D+1}(x) - \widetilde{F}_{D+1}(x) \right| \mathcal{A}_D & \leq (2L_{D+1} + 1) G(D, \tau) + 2 \sup_x \left| \widetilde{F}_{D+1}(x) - F_e(x) \right| \mathcal{A}_D \\
& \leq (2L_{D+1} + 1) G(D, \tau) + \frac{2M^{1/3}(\log D)^{2/3}}{(2D)^{1/3}},
\end{aligned}$$

Combining these results yields

$$\begin{aligned}
& P \left(|F_e(e_{D+1}) - \gamma| \leq \left| \widehat{F}_{D+1}(\widehat{e}_{D+1}) - F_e(\widehat{e}_{D+1}) \right| + \left| F_e(\widehat{e}_{D+1}) - F_e(e_{D+1}) \right| \mathcal{A}_D \right) \\
& \leq \frac{6M^{1/3}(\log D)^{2/3}}{(2D)^{1/3}} + 2(L_{D+1}G(D, \tau) + 2L_{D+1} + 1)G(D, \tau).
\end{aligned}$$

Finally, applying this bound for $\gamma = \beta$ and $\gamma = 1 - \alpha + \beta$ in (A.2) yields the theorem statements

$$\left| P(y_{D+1} \in \mathcal{C}_{D+1}^\alpha | t_{D+1}) - (1 - \alpha) \right| \leq \frac{12M^{1/3}(\log D)^{2/3}}{(2D)^{1/3}} + 4(L_{D+1}G(D, \tau) + 2L_{D+1} + 1)G(D, \tau).$$

□

Lemma A.1. *Under Assumption 3, 4, and 5, with probability at least $1 - \delta$,*

$$\sum_{d=1}^D |\widehat{e}_d - e_d| \leq D \cdot G(D, \tau)^2,$$

where $G(D, \tau)$ is defined as in Equation (1).

Proof. For $d = 1, \dots, D$, we have the decomposition:

$$\begin{aligned}
|\hat{e}_d - e_d| &= \left| \hat{\varepsilon}_d^T \hat{\Sigma}_D^{-1} \hat{\varepsilon}_d - \varepsilon_d^T \Sigma^{-1} \varepsilon_d \right| \\
&\leq \left| \hat{\varepsilon}_d^T \hat{\Sigma}_D^{-1} \hat{\varepsilon}_d - \varepsilon_d^T \hat{\Sigma}_D^{-1} \varepsilon_d \right| + \left| \varepsilon_d^T \hat{\Sigma}_D^{-1} \varepsilon_d - \varepsilon_d^T \Sigma^{-1} \varepsilon_d \right| \\
&\leq \|\hat{\Sigma}_D^{-1}\| \|\hat{\varepsilon}_d - \varepsilon_d\|^2 + \|\varepsilon_d\|^2 \|\hat{\Sigma}_D^{-1} - \Sigma^{-1}\| \\
&\leq \|\hat{\Sigma}_D^{-1}\| \|\hat{\varepsilon}_d - \varepsilon_d\|^2 + \|\varepsilon_d\|^2 \|\hat{\Sigma}_D^{-1}\| \|\Sigma^{-1}\| \|\hat{\Sigma}_D - \Sigma\| \\
&\leq \frac{1}{\lambda} \|\hat{\varepsilon}_d - \varepsilon_d\|^2 + \frac{1}{\lambda^2} \|\varepsilon_d\|^2 \|\hat{\Sigma}_D - \Sigma\|.
\end{aligned} \tag{A.3}$$

By Assumption 5, $\mathbb{E}[\|\varepsilon_d\|^2] \leq c_4 \omega$. Applying Chebyshev's inequality yields

$$P \left(\left| \frac{1}{D} \sum_{d=1}^D \|\varepsilon_d\|^2 - \mathbb{E}[\|\varepsilon_d\|^2] \right| \geq \sqrt{\frac{\text{Var}[\|\varepsilon_d\|^2]}{D\delta}} \right) \leq \frac{\text{Var}[\|\varepsilon_d\|^2]}{D \left(\frac{\text{Var}[\|\varepsilon_d\|^2]}{D\delta} \right)} = \delta.$$

Thus, with probability at least $1 - \delta$

$$\frac{1}{D} \sum_{d=1}^D \|\varepsilon_d\|^2 \leq \mathbb{E}[\|\varepsilon_d\|^2] + \sqrt{\frac{\text{Var}[\|\varepsilon_d\|^2]}{D\delta}} \leq c_4 \omega + \sqrt{\frac{c_5 \omega}{D\delta}}.$$

From Theorem 2.1 in [Chen et al. \(2013\)](#), we have

$$\mathbb{E} \|\hat{\Sigma}_D - \Sigma\|^2 \leq C_1 \left[\left(\sum_{j,k=1}^{n-n'} \min(\tau^2, \sigma_{jk}^2) \right) + (n-n')^2 \min \left(\frac{1}{D}, \frac{\tau^{2-\omega/2}}{D^{\omega/4}}, H(\tau) \right) \right].$$

Applying Chebyshev's inequality,

$$P \left(\|\hat{\Sigma}_D - \Sigma\| \geq \sqrt{\frac{1}{\delta} \mathbb{E} \|\hat{\Sigma}_D - \Sigma\|^2} \right) \leq \frac{\mathbb{E} \|\hat{\Sigma}_D - \Sigma\|^2}{\frac{1}{\delta} \mathbb{E} \|\hat{\Sigma}_D - \Sigma\|^2} = \delta,$$

which means that with probability higher than $1 - \delta$,

$$\|\hat{\Sigma}_D - \Sigma\| \leq \frac{C_1}{\delta} \left[\left(\sum_{j,k=1}^{n-n'} \min(\tau^2, \sigma_{jk}^2) \right) + (n-n')^2 \min \left(\frac{1}{D}, \frac{\tau^{2-\omega/2}}{D^{\omega/4}}, H(\tau) \right) \right]. \tag{A.4}$$

Substituting these bounds into the summation of (A.3), with probability at least $1 - \delta$,

$$\begin{aligned}
&\sum_{d=1}^D |\hat{e}_d - e_d| \\
&\leq D \left\{ \frac{\delta_D^2}{\lambda} + \frac{C_1}{\lambda^2 \delta} (c_4 \omega + \sqrt{\frac{c_5 \omega}{D\delta}}) \left[\left(\sum_{j,k=1}^{n-n'} \min(\tau^2, \sigma_{jk}^2) \right) + (n-n')^2 \min \left(\frac{1}{D}, \frac{\tau^{2-\omega/2}}{D^{\omega/4}}, H(\tau) \right) \right] \right\}.
\end{aligned}$$

□

Lemma A.2. Under Assumptions 3, 4, and 5, with probability at least $1 - \delta$,

$$|\hat{e}_{D+1} - e_{D+1}| \leq G(D, \tau)^2,$$

where $G(D, \tau)$ is defined in Equation (1).

Proof.

$$\begin{aligned} |\hat{e}_{D+1} - e_{D+1}| &= \left| \hat{\varepsilon}_{D+1}^T \hat{\Sigma}_D^{-1} \hat{\varepsilon}_{D+1} - \varepsilon_{D+1}^T \Sigma^{-1} \varepsilon_{D+1} \right| \\ &\leq \left| \hat{\varepsilon}_{D+1}^T \hat{\Sigma}_D^{-1} \hat{\varepsilon}_{D+1} - \varepsilon_{D+1}^T \hat{\Sigma}_D^{-1} \varepsilon_{D+1} \right| + \left| \varepsilon_{D+1}^T \hat{\Sigma}_D^{-1} \varepsilon_{D+1} - \varepsilon_{D+1}^T \Sigma^{-1} \varepsilon_{D+1} \right| \\ &\leq \|\hat{\Sigma}_D^{-1}\| \|\hat{\varepsilon}_{D+1} - \varepsilon_{D+1}\|^2 + \|\varepsilon_{D+1}\|^2 \|\hat{\Sigma}_D^{-1}\| \|\Sigma^{-1}\| \|\hat{\Sigma}_D - \Sigma\| \\ &\leq \frac{\delta_D^2}{\lambda} + \frac{1}{\lambda^2} \|\varepsilon_{D+1}\|^2 \|\hat{\Sigma}_D - \Sigma\|. \end{aligned} \tag{A.5}$$

According to Assumption 5 and Equation (A.4), we have $\|\varepsilon_{D+1}\|^2 \leq c_4 \omega$ and with high probability $1 - \delta$,

$$\begin{aligned} &|\hat{e}_{D+1} - e_{D+1}| \\ &\leq \frac{\delta_D^2}{\lambda} + \frac{C_1 c_4 \omega}{\lambda^2 \delta} \left[\left(\sum_{j,k=1}^{n-n'} \min(\tau^2, \sigma_{jk}^2) \right) + (n - n')^2 \min \left(\frac{1}{D}, \frac{\tau^{2-\omega/2}}{D^{\omega/4}}, H(\tau) \right) \right] \\ &< \frac{\delta_D^2}{\lambda} + \frac{C_1}{\lambda^2 \delta} (c_4 \omega + \sqrt{\frac{c_5 \omega}{D \delta}}) \left[\left(\sum_{j,k=1}^{n-n'} \min(\tau^2, \sigma_{jk}^2) \right) + (n - n')^2 \min \left(\frac{1}{D}, \frac{\tau^{2-\omega/2}}{D^{\omega/4}}, H(\tau) \right) \right] \end{aligned}$$

□

Lemma A.3. Under Assumption 2, 4, and 5, with probability at least $1 - \delta$,

$$|\hat{F}_{D+1}(x) - \tilde{F}_{D+1}(x)| \leq (2L_{D+1} + 1) G(D, \tau) + 2 \sup_x |\tilde{F}_{D+1}(x) - F_e(x)|,$$

where $G(D, \tau)$ is defined in Equation (1).

Proof. Let $\mathcal{S} = \{d : |\hat{e}_d - e_d| \geq G(D, \tau)\}$. From Lemma A.1, we have $|\mathcal{S}| \cdot G(D, \tau) \leq \sum_{d=1}^D |\hat{e}_d - e_d| \leq D \cdot G(D, \tau)^2$, implying $|\mathcal{S}| \leq D \cdot G(D, \tau)$.

We can bound the difference between empirical CDFs using the Lipschitz property of F_e as follows:

$$\begin{aligned}
& \left| \hat{F}_{D+1}(x) - \tilde{F}_{D+1}(x) \right| \\
& \leq \frac{1}{D} \sum_{d=1}^D \left| \mathbb{1}\{\hat{e}_d \leq x\} - \mathbb{1}\{e_d \leq x\} \right| \\
& \leq \frac{1}{D} \left(|\mathcal{S}| + \sum_{d \notin \mathcal{S}} \left| \mathbb{1}\{\hat{e}_d \leq x\} - \mathbb{1}\{e_d \leq x\} \right| \right) \\
& \leq \frac{1}{D} \left(|\mathcal{S}| + \sum_{d \notin \mathcal{S}} \mathbb{1}\{|e_d - x| \leq |\hat{e}_d - e_d|\} \right) \\
& = \frac{1}{D} \left(|\mathcal{S}| + \sum_{d=1}^D \mathbb{1}\{|e_d - x| \leq G(D, \tau)\} \right) \\
& \leq G(D, \tau) + \frac{1}{D} \sum_{d=1}^D \mathbb{1}\{|e_d - x| \leq G(D, \tau)\} \\
& \leq G(D, \tau) + P(|e_{D+1} - x| \leq G(D, \tau)) \\
& \quad + \sup_x \left| \frac{1}{D} \sum_{d=1}^D \mathbb{1}\{|e_d - x| \leq G(D, \tau)\} - P(|e_{D+1} - x| \leq G(D, \tau)) \right| \\
& = G(D, \tau) + [F_e(x + G(D, \tau)) - F_e(x - G(D, \tau))] \\
& \quad + \sup_x \left(\tilde{F}_{D+1}(x + G(D, \tau)) - \tilde{F}_{D+1}(x - G(D, \tau)) \right) \\
& \quad - \left(F_e(x + G(D, \tau)) - F_e(x - G(D, \tau)) \right) \Big| \\
& \leq (2L_{D+1} + 1) G(D, \tau) + 2 \sup_x \left| \tilde{F}_{D+1}(x) - F_e(x) \right|.
\end{aligned}$$

□

B Additional Tables and Figures

This section provides supplementary tables and figures supporting the data description, feature selection, simulation study, and real-data application. Table [B.1](#) summarizes the

geomagnetic response variables and the near-Earth solar-wind and interplanetary magnetic field (IMF) predictors considered in this study. Figures B.1 and B.2 present time-lagged cross-correlations that illustrate dependence among the geomagnetic indices and motivate a joint model and the selection of exogenous solar-wind inputs. Additional simulation results include a representative realization of the underlying stochastic process in Figure B.3 and the full numerical results for $\tilde{D} = 150$ and $\tilde{D} = 300$ in Tables B.2 and B.3. Table B.4 reports supplementary out-of-sample forecasting results for the 24-hour-ahead prediction task across the five geomagnetic indices and the three competing methods.

Table B.1: Summary of geomagnetic response variables and solar-wind predictor variables used in the forecasting analysis.

Variable	Cadence	Range/Unit	Coverage	Source
<i>Responses:</i>				
Kp	3 hr	0–9, thirds	1932–present	GFZ
Dst	1 hr	nT	1957–present	WDC Kyoto
SYM-H	1 min (resampled to 5 min)	nT	1981–present	WDC Kyoto
SME	1 min (resampled to 5 min)	≥ 0 nT	1975–2025	SuperMAG
SMR	1 min (resampled to 5 min)	nT	1972–2025	SuperMAG
<i>Predictors</i>				
B	1 min (resampled to 1 hr)	≥ 0 nT	1981–present	OMNI
Bz	1 min (resampled to 1 hr)	nT	1981–present	OMNI
Vs	1 min (resampled to 1 hr)	≥ 0 km/s	1981–present	OMNI
Pt	1 min (resampled to 1 hr)	≥ 0 K	1981–present	OMNI
Fp	1 min (resampled to 1 hr)	≥ 0 nPa	1981–present	OMNI
Ef	1 min (resampled to 1 hr)	mV/m	1981–present	OMNI

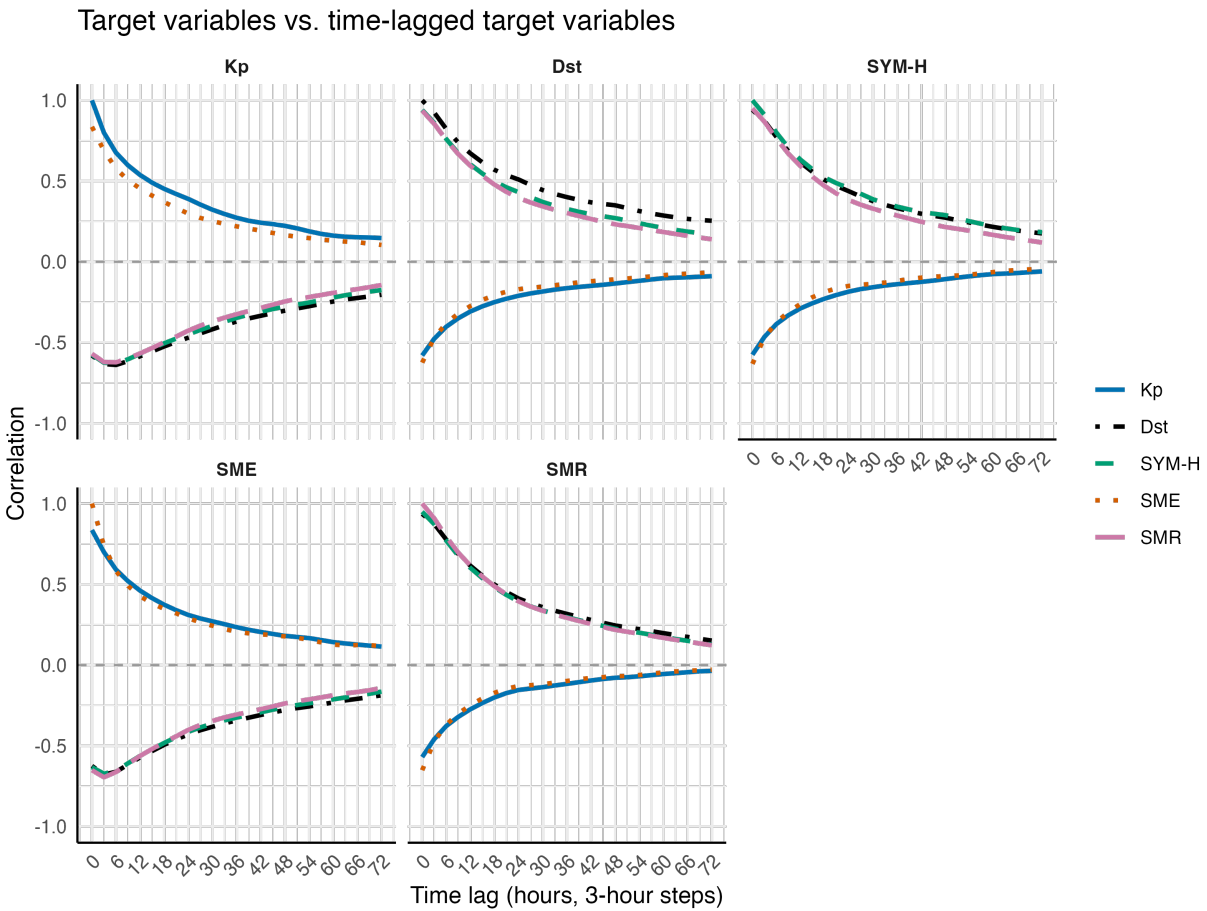


Figure B.1: Time-lagged cross-correlations over lags from 0 to 72 hours among the geomagnetic indices. Each panel corresponds to one lagged geomagnetic index, and the curves show its correlation with the contemporaneous values of Kp, Dst, SYM-H, SME, SMR at 3-hour lag intervals.

Target variables vs. time-lagged OMNI features

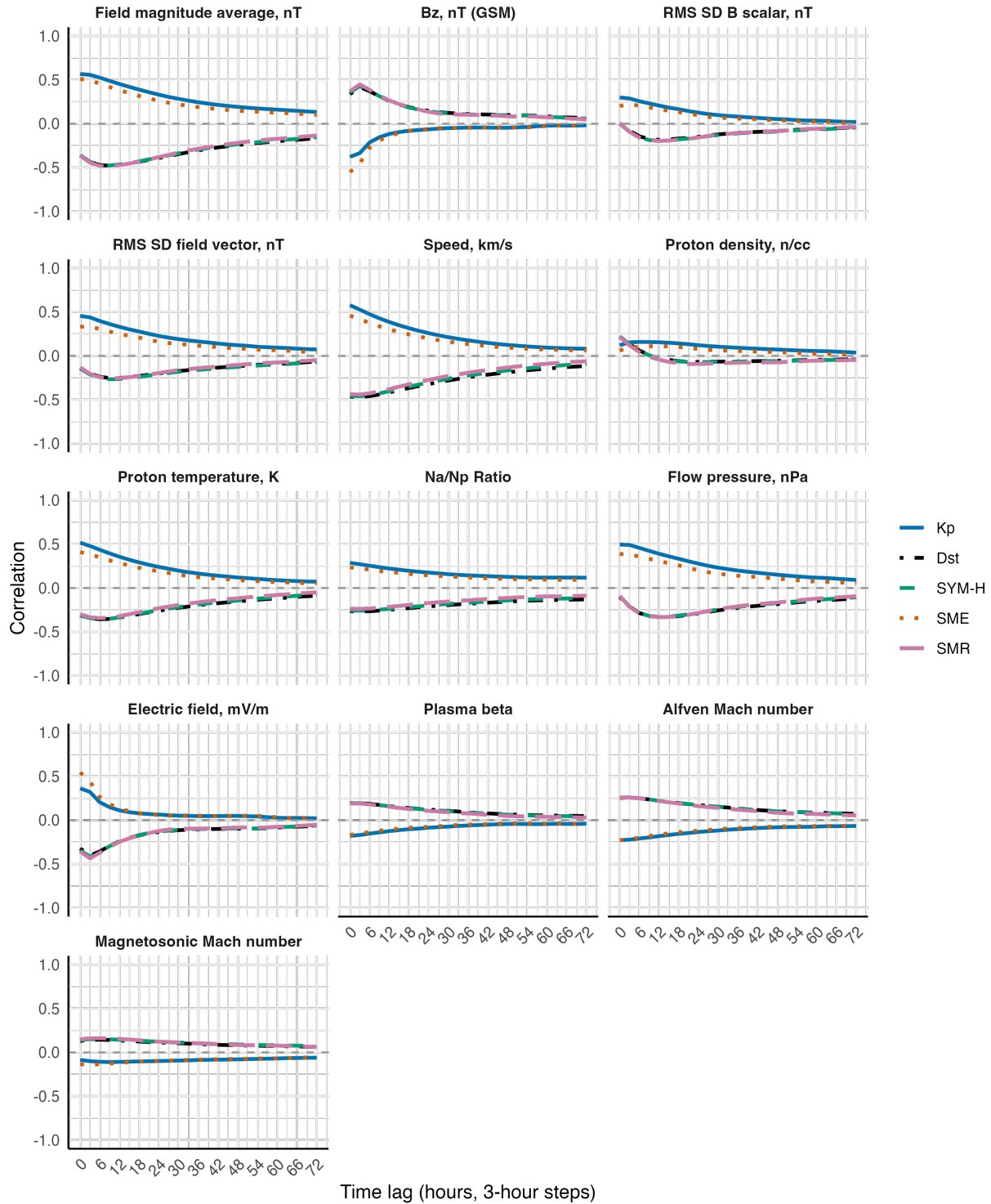


Figure B.2: Time-lagged cross-correlations over lags from 0 to 72 hours between the geomagnetic indices and candidate OMNI solar-wind variables. The observed lagged associations motivated the selection of B (IMF magnitude), Bz (southward IMF component), Vs (solar-wind speed), Pt (proton temperature), Fp (flow pressure), and Ef (motional electric field) as predictors.

Table B.2: Simulation results for $\tilde{D} = 150$ comparing the proposed OLFTSA method under varying overlap ratios (γ) against FSSA, in terms of point forecast accuracy, uncertainty quantification (nominal coverage level 0.95), and computational cost (in minutes). Results are averaged over 10 replications.

n	Method	RMSE	MAE	ECP	MIW	Time
100	OLFTSA ($\gamma = 0.0$)	0.9360	0.7363	0.9367	3.6303	0.0211
	OLFTSA ($\gamma = 0.4$)	0.6133	0.4620	0.9772	2.9030	0.0357
	OLFTSA ($\gamma = 0.6$)	0.6471	0.4968	0.9718	3.1177	0.0674
	OLFTSA ($\gamma = 0.8$)	0.4104	0.3063	0.9671	2.3841	0.2561
	FSSA-Bootstrap	0.6366	0.4924	0.3800	2.3178	1.2164
300	OLFTSA ($\gamma = 0.0$)	1.0235	0.8002	0.9672	4.6424	0.0906
	OLFTSA ($\gamma = 0.4$)	0.7623	0.5810	0.9683	3.7853	0.0975
	OLFTSA ($\gamma = 0.6$)	0.7852	0.6079	0.9657	3.4514	0.1233
	OLFTSA ($\gamma = 0.8$)	0.5681	0.4334	0.9665	3.0029	0.2935
	FSSA-Bootstrap	0.9431	0.7343	0.5218	3.4906	2.3660
500	OLFTSA ($\gamma = 0.0$)	1.1871	0.9300	0.9755	5.9142	0.2971
	OLFTSA ($\gamma = 0.4$)	0.8789	0.6735	0.9825	4.3567	0.2637
	OLFTSA ($\gamma = 0.6$)	0.8607	0.6606	0.9629	3.8488	0.2838
	OLFTSA ($\gamma = 0.8$)	0.6188	0.4718	0.9718	3.2077	0.4695
	FSSA-Bootstrap	1.1844	0.9229	0.5233	4.3782	3.9715

Table B.3: Simulation results for $\tilde{D} = 300$ comparing the proposed OLFTSA method under varying overlap ratios (γ) against FSSA, in terms of point forecast accuracy, uncertainty quantification (nominal coverage level 0.95), and computational cost (in minutes). Results are averaged over 10 replications.

n	Method	RMSE	MAE	ECP	MIW	Time
100	OLFTSA ($\gamma = 0.0$)	0.7924	0.6214	0.9689	3.6233	0.0455
	OLFTSA ($\gamma = 0.4$)	0.5214	0.3990	0.9567	2.2372	0.1002
	OLFTSA ($\gamma = 0.6$)	0.5274	0.3970	0.9737	2.9314	0.2111
	OLFTSA ($\gamma = 0.8$)	0.3869	0.2734	0.9624	2.2238	0.9433
	FSSA-Bootstrap	0.6124	0.4835	0.4134	2.2003	12.6185
300	OLFTSA ($\gamma = 0.0$)	1.0777	0.8487	0.9626	4.6142	0.1373
	OLFTSA ($\gamma = 0.4$)	0.7551	0.5745	0.9564	3.2074	0.1792
	OLFTSA ($\gamma = 0.6$)	0.6633	0.5043	0.9695	3.3165	0.2949
	OLFTSA ($\gamma = 0.8$)	0.4742	0.3468	0.9617	2.6597	1.0961
	FSSA-Bootstrap	0.9824	0.7741	0.5121	3.6702	16.4341
500	OLFTSA ($\gamma = 0.0$)	1.2297	0.9699	0.9597	5.2539	0.3398
	OLFTSA ($\gamma = 0.4$)	0.8895	0.6832	0.9557	3.7466	0.3425
	OLFTSA ($\gamma = 0.6$)	0.7568	0.5801	0.9690	3.6403	0.4520
	OLFTSA ($\gamma = 0.8$)	0.5400	0.4023	0.9638	2.8967	1.2209
	FSSA-Bootstrap	1.3292	1.0616	0.5897	4.8781	22.8012

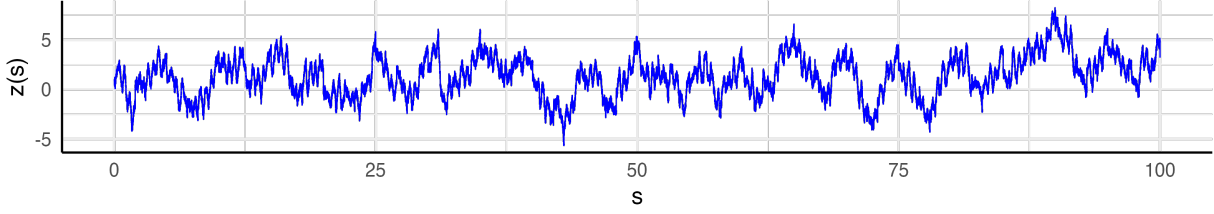


Figure B.3: Example trajectory of the underlying process $z(s)$ over the global time domain.

Table B.4: Performance comparison of 24-hour lead time prediction.

Index	OLFTSA			LSTM			CHRONOS		
	RMSE	MAE	R	RMSE	MAE	R	RMSE	MAE	R
Kp	1.0520	0.8027	0.5899	1.1505	0.9082	0.4630	1.1682	0.8729	0.4909
Dst	13.0899	8.0703	0.7555	15.9709	10.0122	0.6247	15.0583	9.0356	0.6629
SYM-H	13.4627	8.2747	0.7538	17.7221	11.2564	0.6147	16.4369	9.6024	0.6120
SMR	13.5061	8.0424	0.7126	16.4162	9.8411	0.5713	16.2052	8.8930	0.5631
SME	196.2860	133.4225	0.4235	209.2637	152.1024	0.2849	217.5409	134.2652	0.3201